Optimized Profile Retrievals of Aerosol Microphysical Properties from Simulated Spaceborne Multiwavelength Lidar

Daniel Pérez-Ramírez[1,2], David N. Whiteman[3], Igor Veselovskii[4], Mikhail Korenski[4], Peter R. Colarco[5], Arlindo M. da Silva[5]

[1]Applied Physics Department, University of Granada, 18071, Granada, Spain
[2]Andalusian Institute for Earth System Research (IISTA-CEAMA), 18006, Granada, Spain
[3]Atmospheric Sciences Program, Howard University, Washington, DC 20059
[4]Physics Instrumentation Center of the General Physics Institute, Troitsk, Moscow, Russia
[5]NASA Goddard Space Flight Center, 20771, Greenbelt, Maryland, United States.

Correspondence to: Daniel Perez-Ramirez; E-mail: dperez@ugr.es;

ABSTRACT

This work is an expanded study of one previously published on retrievals of aerosol microphysical properties from space-borne multiwavelength lidar measurements. The earlier studies and this one were done in the framework of the NASA Aerosol-Clouds-Ecosystems (now the Aerosol Clouds Convection and Precipitation) NASA mission. The focus here is on the capabilities of a simulated spaceborne multiwavelength lidar system for retrieving aerosol complex refractive index ($m = m_r + im_i$) and spectral single scattering albedo (SSA(λ)), although other bulk parameters such as effective (r_{eff}) radius and particle volume (V) and surface (S) concentrations are also studied. The novelty presented here is the use of recently published, case-dependent optimized-constraints on the microphysical retrievals using three backscattering coefficients (β) at 355, 532 and 1064 nm and two extinction coefficients (α) at 355 and 532 nm, typically known as the stand-alone 3β+2α lidar inversion. Case-dependent optimized-constraints (CDOC) limit the ranges of refractive index, both real (m_r) and imaginary (m_i) parts, and of radii that are permitted in the retrievals. Such constraints are selected directly from the 3β+2α measurements through an analysis of the relationship between spectral dependence of aerosol extinction-to-backscatter ratios (LR) and the Ångström exponent of extinction. The analyses presented here for different sets of size distributions and refractive indices reveal that the direct determination of CDOC are only feasible for cases where the uncertainties in the input optical data are less than 15 %. For the same simulated spaceborne system and yield than in Whiteman et al., (2018), we demonstrated that the use of CDOC as essential for the retrievals of refractive index and also largely improved retrieval of bulk parameters. A discussion of the global representativeness of CDOC is presented using simulated lidar data from a 24-hour satellite track using GEOS model output to initialize the lidar simulator. We found that CDOC are representative of many aerosol mixtures in spite of some outliers (e.g. highly hydrated particles) associated with the assumptions of bimodal size distributions and of the same refractive index for fine and coarse modes. Moreover, sensitivity tests performed using synthetic data reveal that retrievals of imaginary refractive index (m_i) and SSA are extremely sensitive to β(355).

1.- Introduction

Understanding the role of atmospheric aerosols in the Earth-Atmosphere radiative system is essential for improving our knowledge of global change. Atmospheric aerosol particles scatter and absorb solar and near infrared Earth radiation, and also act as cloud condensation nuclei affecting cloud development and precipitation (e.g. Boucher et al., 2013). In spite of the large advances during the last decades in understanding aerosol optical depth (AOD) and aerosol size, there are still uncertainties mainly about aerosol absorption properties (McComiskey et al., 2008; Loeb and Su, 2010), particularly in their vertical distribution (e.g. Zarzycki and Bond, 2010). Advancing our understanding of vertically-resolved aerosol absorption will improve our knowledge of aerosol effects on climate and the capabilities and accuracies in large-scale numerical models (e.g. Stier et al., 2013).

In response to the 2017 National Academy of Science Decadal Survey (https://nas-sites.org/americasclimatechoices/2017-2027-decadal-survey-for-earth-science-and-applications-from-space/) NASA initiated the Aerosol Cloud Convection Precipitation (ACCP) mission study (https://science.nasa.gov/earth-science/decadal-accp). ACCP builds on the heritage of all the studies carried out during the NASA Aerosol, Cloud, Ecosystems (ACE - https://acemission.gsfc.nasa.gov/) mission preparatory stage. ACE was identified as a priority in the 2007 Decadal Survey (https://www.nap.edu/catalog/11820/earth-science-and-applications-from-space-national-imperatives-for-the) and a key aspect in ACE was the deployment of a space-borne lidar system for aerosol vertical-characterization globally, which would also give continuity to previous NASA missions such as CALIPSO (Winker et al., 2010) and CATS (Yorks et al., 2016). ACE mission also used the heritage of other past missions (e.g. GLORY - https://www.nasa.gov/mission_pages/Glory/main/index.html) focused on detecting plausible changes of aerosol radiative forcing and on determining quantitatively the contribution of this forcing to the planetary energy balance (Mischenko et al., 2007). The accuracy requirement for aerosol complex refractive index ($m = m_r + im_i$) and single scattering albedo (SSA) is associated with the need to constrain aerosol chemical composition, which would permit the discrimination between natural and anthropogenic aerosol (e.g. Mischenko et al., 2007). Such accuracy implies to which yield to uncertainties in vertically-resolved aerosol parameters of ±0.05 in m_r, ±50% in m_i, and ±20 % in aerosol absorption coefficient To achieve these accurate measurements, the candidate ACE lidar system was a multiwavelength High Spectral Resolution Lidar (HSRL - Shipley et al., 1983) using the heritage of the NASA Langley HSRL-2 system (Hair et al., 2008; Burton et al., 2018). Such a system allows independent measurements of three backscattering coefficients (β) at 355, 532 and 1064 nm and two extinction (α) coefficients at 355 and 532nm. Aerosol depolarization measurements (δ) at 355, 532 and 1064 nm are also possible. A spaceborne version of this lidar does not exist yet although such an instrument is currently under consideration by NASA for meeting the challenges set out in the 2017 Decadal Survey. The combination of a spaceborne HSRL lidar system with other instruments such as a multiwavelength multi-angle polarimeter, radar and ocean color will provide a unique set of measurements and allows addressing current scientific challenges in the ACCP mission.

Multiwavelength lidar systems have the ability to retrieve aerosol microphysical properties by inverting the 3β+2α measurements (hereafter referred as the stand-alone 3β+2α lidar inversion). The most popular technique for inverting 3β+2α measurements is the well-known regularization technique (e.g. Müller et al., 1999; Veselovskii et al., 2002). Since their first use on lidar measurements improvements have been made in these techniques resulting in more robust and efficient computer codes (e.g. 2-d inversion (Kolgotin and Müller, 2008), linear estimation (Veselovskii et al., 2012), Optimal Estimation (Chemyakin et al., 2014, 2016; Kolgotin et al., 2016)). The regularization technique has been shown to be effective in the retrieval of aerosol bulk parameters such as effective radius (r_{eff}) and particle number (N), surface (S), and volume (V) concentrations with many articles published about the characterization of different aerosol types: biomass-burning (Müller et al., 2005, 2011; Veselovskii et al., 2015), pollution (Noh et al., 2009; Veselovskii et al., 2013) or arctic haze (Müller et al., 2004). The regularization technique was also adapted for the retrieval of non-spherical particles (e.g. Veselovskii et al., 2010) with some publications also studying Saharan dust (e.g. Granados-Muñoz et al., 2016; Veselovskii et al., 2016).

However, the stand-alone 3β+2α lidar inversion has limited information content for independent retrievals of complex refractive index and SSA (Veselovskii et al., 2005; Burton et al., 2016). This implies that the inversion benefits from constraints that are adapted for each individual inversion, as demonstrated by Perez-Ramirez et al., (2019) where the approach showed particular promise. These authors used the large database of AERONET inversions (e.g. Dubovik and King, 2000; Dubovik et al., 2006) to develop case-dependent optimized-constraints (hereafter CDOC) that allowed the retrieval of complex refractive index and SSA with uncertainties remaining within the requirements of the ACE mission (±0.05 in m_r, ±50% in m_i, and ±20 % in aerosol absorption coefficient). In that publication, CDOC were used for retrievals of SSA from HSRL-2 measurements. However, the effect of random and systematic uncertainties on the estimation of case-dependent optimized-constraints and the retrievals was not studied.

In the framework of the ACE mission pre-formulation study a spaceborne lidar simulation study was performed by Whiteman et al., (2018). A large set of different aerosol mixtures was generated by the Goddard Earth Observing System Model, Version 5 (GEOS-5, Rienecker et al. 2008), and the model of Whiteman et al., (2001, 2010) was used to generate simulated spaceborne HSRL measurements. This study also analyzed the yield of the simulated lidar system and studied the possibility of removing some channels in the retrievals of aerosol microphysical properties (e.g. stand-alone $3\beta+1\alpha$ lidar inversion). The inversions were run assuming maximum m_i of 0.01 which did not allow retrievals for cases with significant absorption. The results were not very optimistic as they did not provide reliable retrievals of m_r and many other bulk parameters such as r_{eff} and V were very sensitive to uncertainties in the input optical data although other parameters, such as surface area concentration, proved to be highly resistant to input optical data uncertainties.

The objective of this work is to study the effects of systematic and random uncertainties on the determination of CDOC and the retrieval of aerosol complex refractive index and spectral SSA using those constraints, and also how CDOC can improve retrievals of bulk parameters such as effective radius (r_{eff}) and particle volume (V), surface (S) and number (N) concentrations. To that end, we perform a set of simulations with known aerosol size distribution and refractive indices representative of instances when CDOC can be applied. We also propose a follow-up of the spaceborne simulations done by Whiteman et al., (2018) using the same set of simulated spaceborne lidar measurements but now using CDOC in order to study if such a spaceborne lidar system is capable of retrieving aerosol complex refractive index and SSA, and also aerosol bulk parameters. Detailed discussions of the applicability of CDOC are also presented.

2.- Methodology: Use of case-dependent optimized-constraints in 3β+2α retrievals by regularization

2.1.-Retrievals of aerosol microphysical properties using the regularization technique

The relationships between an ensemble of particle with a given volume size distribution (v(r)) and their extinction and backscattering coefficients is given by the Fredholm equation as (Müller et al., 1999a; Veselovskii et al., 2002):

$$g_j(\lambda_i) = \int_{r_{min}}^{r_{max}} K_{j,V}(m, r, \lambda_i) v(r) dr \qquad (1)$$

Where $g_j(\lambda_i)$ denotes the measured optical data, either the extinction (α) or backscattering (ß) coefficients at wavelength λ_i for a typical lidar system, and $K_{j,V}(m,r,\lambda_i)$ are the wavelength-dependent volume kernel functions based on Mie theory that depend on wavelength and on particle radius 'r' and complex refractive index $m = m_r + im_i$. The regularization technique (Veselovskii et al., 2002) is used to solve Eq. 1, which uses a linear combination of triangular basis functions to reconstruct the size distribution. Because the problem is under-determined the retrieval identifies a group of solutions through a discrepancy parameter (ρ) defined as the difference between input g(λ) and calculated g'(λ) optical data, with the final solution taken as the average of all possible solutions with discrepancy of 1% or less. Note that the use of Mie kernels implies that only spherical particles are considered.

The big limitation of the stand-alone 3β+2α lidar inversion by regularization is the under-determined nature of problem (Veselovskii et al., 2005; Burton et al., 2016), and therefore it is not possible to retrieve independently aerosol size distribution, bulk parameters and refractive indices unless constraints are applied to the retrievals. Actually, the use of constraints in the retrievals is critical for obtaining retrievals of refractive indexes with acceptable uncertainties of ± 0.05 for m_r and 50% for m_i (Pérez-Ramírez et al., 2019). This implies that *a priori* information about the aerosol type is needed. Such additional information can be obtained by using, for example, measurements of aerosol depolarization for aerosol typing (e.g. Burton et al., 2012, 2013, 2014, 2015) or analyzing spectral dependence of extinction-to-backscatter ratio (otherwise known as the lidar ratio, LR) and Ångström exponent of extinction (γ_α) under certain assumptions as we are studying here.

2.2.- Algorithm for the estimation of case-dependent optimized-constraints

The selection of appropriate case-dependent optimized-constraints (CDOC) was described in details in Perez-Ramirez et al., (2019). Firstly, the selection of CDOC was based on the column-average results obtained from the large database of AERONET inversions (Dubovik and King, 2000; Dubovik et al., 2006) that uses sun/sky radiances provides an increase in information content when compared with the $3\beta+2\alpha$ lidar technique. Particularly AERONET Level 2.0 Version 2 was used and we worked with almucantar inversions and with instantaneous measurements. We selected worldwide sites representative of biomass-burning and anthropogenic pollution and we skip inversions with sphericity parameter above 70% to guarantee working with spherical particles. Actually, long-term data from 30 different stations were used with a total of ~15000 inversions. The parameters analyzed were aerosol refractive index and particularly possible relationships between their real and imaginary parts. Results revealed that generally large m_i (> 0.015) were obtained for m_r above 1.45 while small m_i (< 0.075) were obtained for m_r below 1.40 (see Figure 2 in Perez-Ramirez et al., 2019 for more details). The results of limiting m_r with m_i were demonstrated to be consistent with the different aerosol types assumed by the Goddard Chemistry, Aerosol, Radiation, and Transport model (GOCART – Chin et al., 2002). These general relationships were thus used in the determination of the constraints for the stand-alone $3\beta+2\alpha$ lidar inversion to limit the ranges of m_r if *a priori* information about m_i is known. This approach was shown to stabilize the inversion and provides retrievals of aerosol refractive index and SSA within the desired uncertainties. But to be clear, we insist that CDOC were obtained from the analyses of long-term AERONET inversions data for spherical particles, and thus, on average, makes the stand-alone $3\beta+2\alpha$ lidar inversions with CDOC consistent with the AERONET database.

An overview of the procedure to compute CDOC from $3\beta+2\alpha$ measurements is given here. The base is the use of the graphical methods of Figure 1, which represents LR(532 nm) versus LR(355 nm) (Figure 1a) and LR(355 nm)/LR(532 nm) versus γ_α (Figure 1b). Initially is assumed only predominance of fine mode particles and only unimodal size distributions are used in the computations. In Figure 1a we observe different regions computed for r_{modal} = 0.075, 0.10, 0.14, and 0.18 μm and m_i= 0, 0.005, 0.01, 0.025, 0.05 and 0.075, with width of the size distributions σ = 0.4 μm. The graph shown is only representative for m_r = 1.55, but are also computed for m_r = 1.35, 1.45 and 1.65 (not shown for clarity). Dashed lines represent fixed m_i with r_{modal} variable, while continuous lines imply fixed r_{modal} and variable m_i. The plot permits to directly estimate imaginary refractive index (m_i') from spectral LRs measurements under the assumptions of unimodal size distribution.

The graph of Figure 1b shows LR(355 nm)/LR(532 nm) versus γ_α using again unimodal size distribution with r_{modal} = 0.075, 0.10, 0.14, and 0.18 µm, but now varying for different values of real refractive index of m_r = 1.35, 1.45, 1.55 and 1.65. This Figure serves to evaluate the estimated m_i' from Figure 1a. Figure 1b is just an example for the case when m_i' is close to 0.01. Actually, Figure 1b and permits the evaluation of m_i' previously calculated by computing an estimation of the real refractive index (m_r'): if the difference between m_r' and the value used in Figure 1a (1.55 in our case) is larger than ±0.05, then m_i' is rejected and assumed as not valid.

But the graphical methods of Figure 1 must be used carefully. In Figure 1a different m_i' are obtained when varying the assumed m_r in plot computations. Similar happens in Figure 1b when varying the assumed m_i. To solve these issues, we propose a step-by-step procedure that consists of repeating the procedure described in the previous paragraph for m_r = 1.35, 1.45 and 1.65, which consequently imply re-computing both plots in each step: Each assumed m_r will provide an estimate of m_i' that later is used to compute its corresponding Figure 1b. Once Figure 1b is built with m_i close to m_i' the computation of m_r' is possible and finally m_i' is evaluated with the condition $m_r - m_r' \leq \pm 0.05$. That can provide up to four different pairs of (m_r', m_i'), and from the pairs not rejected the average m_i' is computed and denoted as $m_{i,optimized}$. AERONET derived relationships between m_i and m_r are used to compute the optimized real refractive index ($m_{r,optimized}$,). Such values of $m_{i,optimized}$ and $m_{r,optimized}$ together with the initial estimation of fine mode predominance serve eventually as the CDOC: Determination of $m_{i,max}$ allowed in the inversion as 2.5$m_{i,optimized}$, limitation of m_r within $m_{r,optimized}$±0.05, and maximum range of radius allowed in the inversion up to 2 µm (details in Perez-Ramirez et al., 2019).

However, with the previous step-by-step procedure is possible that the four different pairs (m_r', m_i') are rejected and consequently imply that the assumption of fine mode predominance is not fulfilled. Therefore, the aerosol size distribution is now assumed as bimodal with relevance of coarse mode particles. But we insist here that our approach is only for spherical particles, and this coarse mode is either representative of the residual coarse mode observed in AERONET for biomass-burning or pollution events (Dubovik et al., 2002) or for the presence of marine aerosol particles (coarse particle with residual fine mode). Nevertheless, there could be possible that such mixtures present large m_i (e.g. larger than 0.01) and we developed a graphical method that consists of plotting LR(532 nm) versus LR(355 nm) for the same sets of m_i than in Figure 1 but varying the ratio between fine and coarse mode in the range 0.1-2. Our analyses revealed that computation of m_i' for m_r = 1.55 was representative of any mixture (see Fig.6 in Pérez-Ramírez et al., 2019) and thus serves for a direct computation of $m_{i,optimized}$. CDOC were computed with $m_{i,max}$= 2.5$m_{i,optimized}$ and maximum radius allowed of 10 µm. No limitations in m_r are assumed in mixtures.

[Insert Figure 1 here]

The algorithm to determine CDOC was demonstrated as consistent when applied to NASA Langley HSRL-2 system (Hair et al., 2008; Burton et al., 2018) and compared with aerosol typing from spectral depolarization analyses (Burton et al., 2012, 2013, 2014) during DISCOVER-AQ field campaigns (https://www-air.larc.nasa.gov/missions/discover-aq/discover-aq.html): urban polluted aerosol at high relative humidity and consequently low absorbing was classified as fine mode predominance and low-absorbing aerosol, while fresh and dry biomass-burning was classified as fine mode predominance and medium-absorbing aerosol. Finally aged-biomass burning was classified as mixture of fine and coarse mode and medium absorbing aerosol. Moreover, during DISCOVER-AQ was possible to analyze retrievals of SSA with CDOC using HSRL-2 with correlative in-situ measurement onboard airborne platforms and the comparison revealed that differences were within the uncertainties expected in each methodology. However, the sensitivity of the algorithm to determine CDOC to random and systematic uncertainties was not study, and to that end we perform in this work consequent analyses on this issue.

3.-Results

3.1. Effects of random uncertainties in the retrievals of aerosol refractive index and single scattering albedo from stand-alone 3β+2α lidar inversion using case-dependent, optimized constraints.

The sensitivity of the CDOC algorithm to varying levels of random uncertainty is studied here using synthetically generated 3β+2α measurements and then adding random uncertainties.

The assumed aerosol size distributions for generating these synthetic measurements were unimodal and representative of a fine mode predominance with r_{modal} = 0.08, 0.10, 0.12, 0.,14 and 0.16μm, with m_r = 1.35, 1.45, 1.55, 1.65 and m_i = 0.001, 0.005, 0.01, 0.025, 0.05 and 0.075. Also, for cases representing both fine and coarse mode, bimodal size distributions were used with fine mode at r_{fine} = 0.14 μm and σ_{fine} =0.4 μm, coarse mode at r_{coarse} = 1.5 μm and with σ_{coarse} =0.6 μm and V_f/V_c of 2, 1, 0.5, 0.2 and 0.1. In these bimodal size distributions refractive indices used were m_r = 1.35, 1.45, 1.55 and 1.65 and m_i = 0.001, 0.005, 0.01, 0.02, 0.025, 0.03. These size distributions are representative of most of the situations obtained from AERONET retrievals (e.g. Dubovik et al., 2002): unimodal size distributions are representative of cases with only fine mode (e.g. pollution). Bimodal size distributions are representative of some biomass-burning cases that present a residual coarse mode (e.g. V_f/V_c = 2) and also of marine aerosol that present a residual coarse mode (e.g. V_f/V_c = 0.2). Cases with only predominance of coarse mode are mostly typical of dust particles (non-spherical particles) that are not included in our analyses. Uncertainties were generated using a random number generator that follows Gaussian distribution centered at zero with width according to the value of the random uncertainty desired, and with a total of 10 000 random numbers representative of that Gaussian distribution. These random numbers were representative of uncertainties in the optical data, and were applied for each optical channel individually assuming no correlation among them. The same procedure is later applied for the other channels but the initiation of the random number generator was different in order to avoid the situation where all the random numbers were the same. After adding random uncertainties to the corresponding optical data, the algorithm for determining CDOC was then applied. Nevertheless, in a real system there could be some kind of dependences between optical channels accuracies with different sensitivities to error in the optical data (e.g. in a real system accuracy in extinction is generally lower than in backscattering), which will require specific analyses when dealing with an specific lidar system.

The results are summarized in Table 1 for the cases of 5, 10, 20, 30 and 50 % random uncertainties in the optical data. For simplicity, we present the results in five different groups depending on the size distributions and m_i used for generating the $3\beta+2\alpha$ measurements: fine mode and low absorption where input $m_i \leq 0.01$, fine mode and medium absorption with $0.01 < m_i < 0.04$, and finally fine mode and high absorption with input $m_i \geq 0.04$. Also, for mixtures when both modes show significant presence, we separate between low absorption ($m_i < 0.01$) and medium absorption ($0.01 < m_i < 0.04$). We do not expect very large absorption in mixtures ($m_i > 0.04$) because such cases in our approach would correspond to a large presence of black carbon that is only realistic for a strong predominance of fine particles (e.g. Chin et al., 2002). The estimation of CDOC is considered to have operated correctly if the datum is classified in its original range of inversion. An overview of the results is given in Table 1which shows the mean percentages of data classified in each group after adding random uncertainties to the input optical data. We do not include 0% random uncertainty in the tables for inputs with no random uncertainty since, with no added uncertainty, the correct selection of case is made 100% of the time.

[Insert Table 1 here]

Table 1 clearly indicates that for every aerosol type the success in determining the correct aerosol type decreases as random uncertainties increase. Initially, we establish the allowable amount of uncertainty when the percentage of data classified correctly is close to one standard deviation. For random uncertainties of 5% all cases are well classified (percentages above 90%), although with lower percentages (~80%) for mixtures with low absorption due to the difficulties associated with the retrieval of mixtures of particles (e.g. Dubovik et al., 2000; Pérez-Ramírez et al., 2015). For 10 % random uncertainties the percentages are around 70-75% for all cases. However, for random uncertainty larger than 20 % the degradation in the aerosol classification becomes quite significant in general with some aerosol types being classified better than others. Dealing with uncertainties larger than 20% implies several limitations in the aerosol classification that eventually affects the retrieved parameters. More specifically, for fine mode predominance with low absorption the percentage of cases classified as low absorbing mixtures increases, which is critical for constraining the range of radii that eventually affects the retrieval of bulk parameters such as volume concentration (Pérez-Ramírez et al., 2013). For fine mode predominance with medium and high absorption the incorrect classification as low absorption will not allow retrievals of high values of m_i (> 0.01) and of low SSA (< 0.95). Finally, mixtures of aerosol types in the presence of larger uncertainties in the optical data yield larger deviations with many points classified as fine mode and low absorption increases. The failure of the algorithm in the classification of mixtures is explained by the fact that large random uncertainties in the optical data cause an incorrect interpretation of the spectral dependence in LRs.

The full impact of random uncertainties on the retrieval of aerosol complex refractive index and spectral SSA is studied by evaluating the stand-alone 3β+2α lidar inversion with CDOC using simulated optical data affected by varying amounts of random uncertainty. The results with error-free data are used as reference. Mean differences between these two sets of inversions are computed, with the results summarized in Table 2 for random uncertainties of 5, 10, 15, 20 and 50%. Note that because we are comparing with noise-free data results only indicate deviation of the retrievals with noise in the input optical data. Accuracy for the retrievals was studied in Perez-Ramirez et al., (2019) and differences between retrievals and input values from size distributions, refractive indexes and SSA were within the uncertainties only when using CDOC. We also recall that according to ACE science white paper acceptable uncertainties in m_r are of ±0.05, while for m_i they are of approximately ±50 % (approximately ±0.005, ±0.01 and ±0.025 for low, medium and high absorption, respectively). If we take 20% as the upper limit uncertainty in absorption coefficient, the corresponding uncertainties in SSA become ±0.02, ±0.04 and ±0.05 for low, medium and high absorption, respectively.

We note that due to the limited information content (Veselovskii et al., 2005) spectral dependence of refractive index cannot be obtained, and the code internally assumes flat refractive index in the retrieval procedure (Veselovskii et al., 2002, 2004). That assumption directly implies a limitation of the retrieval. Nevertheless, according to the literature spectral dependence in retrieved imaginary refracted index is minimum for fine mode particles, while can be important for non-spherical particles such as mineral dust (Dubovik et al., 2002). Because we are working with spherical particles, our assumption of flat refractive index with wavelength is minimized. Nevertheless, all these limitations, together with the limitations to retrieve coarse mode of size distribution (Whiteman et al., 2018), imply also limitations in the spectral retrieval of SSA: for fine mode predominance SSA retrievals are only acceptable at 355 and 532 nm, while they degrade as coarse mode increase implying better retrievals at 1064 nm (see Figures 7 and 8 in Perez-Ramirez et al., 2019 for details)

[Insert Table 2 here]

Table 2 shows that mean differences are below the allowed uncertainties of each parameter for random uncertainties up to 10%. For 15% uncertainties deviations in retrieved parameters are in the middle and are acceptable for the established thresholds. For random uncertainties larger than 20% the retrievals clearly fail for all parameters as is observed in the mean differences for random uncertainties of 50%. Therefore, random uncertainties must be below 15% to guarantee successful retrievals of aerosol refractive index and single scattering albedo.

3.2. Effects of systematic uncertainties in the input optical data on the stand-alone 3β+2α lidar inversion using case-dependent optimized constraints.

The impact of systematic uncertainties on the retrievals of aerosol bulk parameters using the stand-alone 3β+2α lidar inversion was studied in Perez-Ramirez et al., (2013) for spherical and low-absorbing particles ($m_{i,max}$ = 0.01) using a fixed set of inversion constraints. Here we extend those analyses by using CDOC, and in particular we focus on how systematic uncertainties affect the retrieval of aerosol refractive index and spectral SSA.

For the fine mode predominant cases we use the same sets of r_{modal} and refractive indexes as in the simulations for studying the effects of random errors. For simplicity we show the results for r_{modal} = 0.14 μm and for three different m_i representative of low (m_i = 0.005), medium (m_i = 0.025) and high (m_i = 0.05) absorptions. From these size distributions, optical data 3β+2α are generated using Mie theory. Later, we run the stand-alone lidar inversion using CDOC and obtain the retrieved microphysical parameters 'X_{ret}'. In the approach followed we compute CDOC for free-noise data and applied these constraints when biases are applied to optical data. Comparisons of retrieved values with CDOC for free-noise data with reference was done in Perez-Ramirez et al., (2019) and differences were within uncertainties. Thus, the evaluations presented here of comparing free-noise data with noisy data will serve to evaluate the degradation of retrieved parameters.

The procedure for evaluating the effects of systematic uncertainties consists of applying a systematic bias, denoted as Δε, to one optical datum at a time. The bias varies from -30% to +30% in 10 intervals, and this is repeated for each of the 5 optical data. For each of these induced biases, a new set of microphysical parameters X_{bias}, is then obtained. The comparisons are expressed as the percentage difference $\Delta X = 100\cdot(X_{bias}-X_{ret})/X_{ret}$, where 'X' corresponds to bulk parameters (r_{eff}, V, S and N) and also to m_i. For m_r and spectral SSA we use instead $\Delta X = X_{bias} - X_{ret}$.

Figure 2 shows the results of ΔSSA at 355 nm for low, medium and high absorbing cases. The focus is on 355 nm because this is the wavelength where earlier studies have indicated that SSA retrievals for fine mode predominance are more reliable (Perez-Ramirez et al., 2019). The error bars indicate one standard deviation after averaging the four different values of m_r used in the retrievals, and to make Figure 2 more legible we only plot the error bars for β(355) - the error bars for the other quantities are similar or even lower in magnitude. Approximately linear patterns in the deviations of ΔSSA versus bias in the optical data are observed. But the most important result here is that for biases of up to 30% in the input data, the associated deviations in SSA are within the desired range. The sole exception is β(355), which is shown thicker to remark the large sensitivity of SSA retrievals to errors in β(355). The errors in SSA also show significant sensitivity to biases in β(532) for medium absorbing cases and α(355) for high absorbing cases although still the errors stay within the desired limits for biases up to ±30%. Scattering and absorption cross-sections present larger dependence to imaginary refractive index than extinction cross-sections (e.g. Bohren and Huffman, 1998: Mischenko et al., 2002), which could explain the larger sensitivity to errors in the input optical data for SSA retrievals. Moreover, backscattering cross sections are proportional to λ^{-4} (Kovalev and Eichinger, 2004), which could explain the larger sensitivity to bias in β(355). The large sensitivity of errors in SSA to bias in the β(355) measurement is added now to the information regarding biases in bulk parameter inversions that were studied in Pérez-Ramírez et al., (2013), where the only optical inputs showing significant sensitivity to systematic uncertainty were the extinction coefficients.

For cases with fine mode predominance, Table 3 summarizes the standard deviations in ΔSSA when biases in the optical data are applied. Minima are associated with the results using optical data that are the least sensitive to uncertainties, while maxima are associated with the results using the most sensitive optical data. The results indicate than these standard deviations are above the admitted uncertainties in SSA for uncertainties above 15%. Therefore, the analyses of systematic uncertainties are consistent with the previous finding of section 3.1 and we conclude that in general uncertainties must be below 15%. Note that standard deviations for retrieved SSA at 1064 nm are similar to these for other wavelengths, which combined with the failure of SSA retrievals at 1064 nm for noise-free data (see Figure 7 in Perez-Ramirez et al., 2019) is an intrinsic limitation of the stand-alone 3β+2α lidar inversion for fine mode particles predominance, probably associated with the limited information content (Veselovskii et al., 2005).

[Insert Figure 2 here]

[Insert Table 3 here]

For the cases of mixtures of both fine and coarse mode the same scheme has been applied: simulations were performed for a bimodal size distribution with fine mode r_{fine} = 0.14 μm, σ_{fine} =0.4 μm and coarse mode r_{coarse} = 1.5 μm,σ_{coarse} =0.6 μm. But for simplicity we only show the results for imaginary refractive indices of 0.005 and 0.025 representing low and medium absorption, respectively. Simulations were then done for two different fine-to-coarse volume ratios V_f/V_c of 1 (mostly fine mode) and 0.2 (mostly coarse mode). Results of these sensitivity studies for SSA are shown in Figure 3. We only represent results for SSA at 532 and 1064 nm because of the limitations for retrievals at 355 nm in mixture of particles cases (see Figure 8 in Perez-Ramirez et al., 2019 that reveals a failure of the inversion in SSA retrieval at 355 in the cases of mixtures of fine and coarse mode). The standard deviations associated with the inversion of the simulation at different m_r are represented only for β(355) and α(355) for clarity.

[Insert Figure 2 here]

Figure 3 illustrates again approximately linear patterns of ΔSSA versus biases in the optical data. However, there are dependencies with size distribution and input refractive index: for m_i = 0.005 we find that systematic uncertainties in β(355) have the largest influence on derived SSA(532), although ΔSSA stays within the desired uncertainties (±0.02) with uncertainties as large as ±30%. However, with SSA(1064) systematic uncertainties larger than approximately 10% cause deviations that go beyond the desired range of ±0.02. The effects of biases in α(355) in SSA(1064) are not negligible for V_f/V_c = 1, although the deviations are close to the limit. On the other hand, for m_i = 0.025 increases in ΔSSA with the same input biases are clearly observed, and again β(355) is the most sensitive parameter, both for 532 and 1064 nm.

However, sensitivity to α(355) becomes critical for these higher absorbing cases, with larger standard deviations compared to other optical data. Sensitivity to α(532) is also important for $V_f/V_c = 0.2$, but with opposite signs between SSA at 532 and at 1064 nm.

A summary of the study of sensitivities of SSA retrievals to systematic uncertainties in the input optical data for mixtures of fine and coarse particles is given in Table 4. The standard deviations are given for each range of biases in optical data. Again, the minima are associated with the least sensitive optical datum and the maxima with the most sensitive. We also include the standard deviations for SSA(355). From Table 4 it can be seen that in almost all cases for systematic uncertainties up to 15% (and for most cases up to 20%) deviations in the retrieved SSA remain below the desired limit of ±0.02. For larger biases, however, deviations from the reference are only below uncertainties for 532 nm independently of the range of absorption, while for 355 and 1064 nm this is only observed for low absorption. These results illustrate again that CDOC provide generally reliable results for systematic uncertainties up to approximately 15% as observed previously in fine mode predominance, and under certain circumstances larger biases can be tolerated. Note now that standard deviations for ΔSSA at 355 nm are similar to these for 1064 nm, which indicates a stability of the retrieval and could imply that the lack of accuracy in SSA at 355 nm for mixtures is associated with the limited information content of the measurements and perhaps of the retrieval technique as well.

[Insert Table 4 here]

For studying the effects of systematic uncertainties on the retrieval of aerosol refractive index, the same procedure is followed separately for m_r and m_i. As an illustration, Figure 4 shows Δm_r and Δm_i for the case of fine mode predominance and medium absorption. From Figure 3 can be observed that for m_r the extinction coefficients are the most sensitive parameters, although the effects of β(1064) are not negligible. For m_i, β(355) measurements are the most critical, although overestimations of β(532) are not negligible. But the most important point is that the observed deviations are always within the desired limits (±0.05 for m_r and approximately 0.01 for m_i in this case of medium absorption) for biases up to ±30%. However, now the standard deviations are of the same magnitude as the deviations and they must be taken into account in the final error estimation. For m_r the sum of mean deviation plus standard deviations is above the uncertainties (±0.05) for biases above ±20%, and the same is observed for m_i. We also note that additional evaluations revealed very similar patterns after changing the range of absorption and the type of size distribution in the simulation of optical data (graphs not shown for brevity).

[Insert Figure 4 here]

For bulk parameters such as r_{eff}, V, S and N the same study was done and again generally linear patterns are observed for $\Delta x = (x_{bias} - x_{ret})/x_{ret}$ for all the ranges of absorption (graphs not shown for brevity). As summary, the slopes of the linear fits are given in Table 5 for fine mode predominance and for each range of absorption. Positive slopes indicate lower values of bulk parameters when the optical data are affected by negative biases versus when they are not affected by biases, while for positive slopes just the opposite occurs. In Table 5 changes in the slopes of the linear fits are observed when going from low to medium/high absorptions. But the changes are only limited to the absolute value of slopes being generally higher for high absorption.

[Insert Table 5 here]

The most important result from Table 5 is that the most sensitive optical channels to biases are the extinction coefficients in agreement with the results presented in Perez-Ramirez et al., (2013) for non-absorbing aerosol. This last result reveals that there are no relevant changes in the sensitivity to biases in the optical data for the bulk parameters, which is sensible because the use of CDOC in the retrieval of bulk parameters is not critical. Surface concentration is relatively insensitive to changes in absorption range. Particle volume is the least sensitive to biases in optical data. Number concentration, however, is the most sensitive to these biases. For r_{eff}, the sensitivity is in the middle between number and volume concentration, and the most important is that the sign of the slopes for extinction coefficients are in opposite to those in number, surface and volume concentrations. Finally, additional evaluations of bulk parameters for cases when the input size distribution is a mixture of fine and coarse mode revealed very similar results to those of Table 5.

As was done previously in Perez-Ramirez et al, (2013), we next considered whether the combination of systematic uncertainties in the optical data for several channels reproduces the results of the analyses presented in section 3.2 for random uncertainties. That is, we try to answer the question about the additivity of the generally linear patterns observed for biases due to systematic uncertainties. To that end, we studied the differences between deviations in retrieved parameters affected by random uncertainties and deviations computed using the linear patterns resulting from systematic biases. Our results showed no significant differences which is an indication of the additivity of the differences when optical data are affected by biases.

3.3. Case-dependent optimized-constraints applied to GEOS: Study of aerosol hygroscopicity.

For the evaluation of the algorithm for determining CDOC of Section 3.1 for retrievals of different aerosol types we used the special aerosol study cases generated by the Goddard Earth Observing System Model, Version 5 (GEOS, Rienecker et al. 2008). GEOS incorporates the GOCART model (Chin et al., 2002) for simulating different aerosol types (sulphate, organic carbon, black carbon, and sea salt) with dust assumed as a non-spherical specie (Colarco et al., 2014) and excluded in our analyses. GEOS also includes an atmospheric general circulation model, representations of atmospheric physics including moist processes and chemistry. Particularly, a GEOS nature run was used for a 24-hr track of the CALIPSO satellite from July 15, 2009, which provided a total of 8640 profiles, each one with 72 different levels of altitude. Details of these GEOS simulations are in Whiteman et al., (2018).

An important effect to evaluate is that of relative humidity because of the internal assumptions in GOCART: The shape of the size distribution does not change as a function of relative humidity, but there is a displacement of modal radius toward larger radii as relative humidity increases, while the width of the size distribution remains the same. Also, for fine mode predominance particles such as sulphate, organic carbon and black carbon GOCART imposes a strict threshold on size such that no particles with radii above 0.5µm are included, independent of any hygroscopic size increase. Refractive indices of the size distributions affected by hygroscopic growth do indeed change, with m_r decreasing to values close to 1.35 and m_i to values almost negligible (below 0.005) as relative humidity increases to values close to 99%. Details of the effects of relative humidity on aerosol size distribution in GOCART can be consulted in Table 2 of Chin et al., (2002).

Here we evaluate if the algorithm for determining CDOC is useful in these aerosol cases highly affected by relative humidity in GEOS simulations. Figure 5 shows the differences between the imaginary refractive index given by GEOS ($m_{i,GEOS}$) versus $m_{i,optimized}$ computed from the algorithm of section 3.1 using 3β+2α measurements from GEOS data. The differences are represented versus $m_{i,optimized}$, and we divide the results into four different categories: no limitations on relative humidity (Figure 5a) and with relative humidity below 90% (Figure 5b), 75% (Figure 5c) and 50% (Figure 5d). The dashed lines represent the $\pm 2.5 m_{i,optimized}$ which is assumed to be the appropriate value of $m_{i,max}$ for optimizing the stand-alone 3β+2α lidar inversion (Perez-Ramirez et al., 2019). We have skipped in our analysis cases with a large percentage of dust and also of large sea salt particles because the stand-alone 3β+2α lidar inversion is not capable of retrieving properties of such big particles due to limitations in information content (Whiteman et al., 2018).

[Insert Figure 5 here]

Figure 5 reveals that when no limitations are applied on relative humidity approximately 121 cases over 1137 give $m_{i,GEOS}$ - $m_{i,optimized}$ greater than ± 2.5 $m_{i,GEOS}$. These 121 cases typically present $m_{i,optimized} < 0.005$ and $m_{i,GEOS} > 0.01$. However, the number of failures cases applying CDOC is reduced when limiting relative humidity (94, 91 and 28 for thresholds of 90, 75 and 50% RH, respectively). We therefore conclude that CDOC have limitations for the assumptions in GOCART when aerosol is affected by hygroscopicity.

To better understand the effects of relative humidity on $m_{i,optimized}$ we have performed additional simulations with different aerosol size distributions that can be representative for aerosol hygroscopicity. Particularly, for different monomodal size distributions we computed 3β+2α data using Mie theory. Such a set of simulated measurements were used to compute LR355, LR532 and γ_α which were then used as inputs to the algorithm described in section 3.1 and eventually provides CDOC. Results are summarized in Table 6 for size distributions with r_{modal} = 0.12, 0.16, 0.20, 0.25 and 0.30 µm, and σ = 0.4, 0.6 and 0.8 µm. Imaginary refractive index used was of 0.005 representative of no-absorption while m_r was 1.35, representative of highly hydrated aerosol (except for r_{modal} = 0.12 that assumes m_r = 1.45 typical of non-absorbing and non-hydrated particles).

[Insert Table 6 here]

The simulations in Table 6 help us to understand the effect on determining CDOC (based on the algorithm described in section 2.2) to different assumptions for changes in size distributions with aerosol hygroscopic growth: Initially, the dry size distribution can be assumed for r_{modal} = 0.12 µm. Hygroscopic growth implies bigger particles and the simplest approach to achieve that is to just assume a displacement of the r_{modal} to larger values keeping the width of the distribution, σ, the same. Under such assumptions, results of Table 6 show that for r_{modal}> 0.20 µm the algorithm of section 2.2 for determining CDOC fails. The second approach to account for aerosol hygroscopicity assumes that particles below the detection limit for the 3β+2α technique also grow and become detectable, implying a larger width of the size distributions. These size distributions with larger width do not provide appropriate aerosol classification for r_{modal} ≥ 0.20 µm. Nevertheless, if wider size distributions are assumed as consequence of hygroscopic growth r_{modal} ≥ 0.20 µm should be less frequent and thus not affecting critically to the retrievals.

Based on the preceding discussion we can better understand the reasons that data are rejected from Figure 5. Actually, from that Figure cases with relative humidity > 75 % and low absorption (i.e. the mean m_i obtained is 0.005 ± 0.003) microphysical (from GOCART) parameters were very stable, with mean values of r_{eff} = 0.26 ± 0.07 µm and m_r = 1.38 ± 0.02, typical of hydrated particles. The input parameters for the algorithm of section 2.2 have mean values of γ_α = 0.76 ± 0.21, LR_{355} = 87 ± 7sr and LR_{532} = 87 ± 9 sr. CDOC provided mixtures (either low or medium absorptions) or fine mode predominance with medium and high absorption, which consequently is incorrect according to their values from GOCART. Similar results were obtained when limiting relative humidity> 0.90 but with lower mean values of γ_α (0.65 ± 0.18) and higher lidar ratios (LR_{355} = 89 ± 5 sr and LR_{532} = 93 ± 7 sr). These results together with the simulations analysed in Table 6 reveal that the algorithm for determining CDOC constraints does not work appropriately for hydrated aerosols following the approaches considered in this manuscript. For these reasons we skip highly hydrated aerosol (typically, RH >80%) in the following section.

3.4. –The impact of case-dependent optimized-constraints on retrievals from a simulated space-borne HSRL lidar system

To better quantify the performance of the CDOC in the retrieval of the vertical profile of aerosol microphysics, we first study the retrievals directly from the GEOS simulations themselves which amounts to an error-free simulation of lidar performance. To that end, we remove the outliers from Figure 5 (typically for RH >80%) and study differences between retrieved and GEOS-5 values of all aerosol microphysical properties. The metrics used here for quantifying differences between retrieved and reference values are the same as in Whiteman et al., (2018). For example, for bulk parameter deviations is a root-mean-square value calculated as a percentage as:

$$\frac{100}{N}\frac{\sum\sqrt{(X_{GEOS}-X_{ret})^2}}{X_{ret}} \qquad (2)$$

where X_{GEOS} is the reference bulk parameter from GEOS-5 and X_{ret} is the retrieved bulk parameter using CDOC in the3β+2α lidar inversion. N is the total number of data in the computation of the root-mean-squares. For aerosol refractive index and single scattering albedo, we calculate the fractional deviation metric as:

$$\frac{\sum\sqrt{(X_{GEOS}-X_{ret})^2}}{N} \qquad (3)$$

Eqs. (2) and (3) were evaluated for each individual retrieval run with CDOC constraints, and the composite values are summarized in Table 7. We separate again among three different ranges of absorption for clarity: low absorption with $m_i \leq 0.01$, medium absorption with $0.01 < m_i < 0.04$ and high absorption with $m_i \geq 0.04$. Deviations are color-coded based on the magnitude of the deviation. Details of each color-code are summarized in Table 8. We note that Table 8 is very similar to Table 6 presented in Whiteman et al., (2018) but with the particularity that Table 8 provides color-code discrimination for different ranges of m_i and also for SSA at different ranges of m_i. The color thresholds used for bulk parameters are related to the uncertainties described in the ACE mission draft report.

[Insert Table 7 here]

[Insert Table 8 here]

The main result from Table 7 is the capacity of the stand-alone 3β+2α lidar inversion with CDOC to retrieve aerosol microphysical properties for different aerosol types and mixtures when applied to noise-free data. This statement is supported because most retrievals are 'green' independently of the absorption range. We note that the outputs from GEOS do not provide information separately about fine or coarse mode but rather only the total mass of each species. We could argue that sulphate and carbonaceous species are fine mode while dust and sea salt species are coarse mode. But from real AERONET observations pollution and biomass-burning can have a residual coarse mode, and similarly sea salt and dust can have a residual fine mode (e.g. Dubovik et al., 2002). For these reasons we did not perform any separation between fine modes and mixtures using GEOS data, although the influence of fine mode is always large because we are skipping mineral dust in our analyses and the majority of the cases in the simulation present important contributions of sulphate and carbonaceous species. Nevertheless, the results presented here show a large improvement when compared with those of Whiteman et al., (2018) (c.f. Table 4) who evaluated the stand-alone 3β+2α lidar inversion from GEOS data limiting the maximum imaginary refractive index to 0.01 and without using case-dependent constraints as used here. The only important failure is in the retrieval of SSA at 1064 nm because of the lack of accuracy of the stand-alone 3β+2α lidar inversion in the retrieval of SSA at 1064 nm for aerosol for fine mode predominance (Perez-Ramirez et al., 2019) that as commented has important influence in the database used for the simulations.

The stand-alone 3β+2α lidar inversion with CDOC for a simulated ACE lidar system is performed here. Details of the simulated space-borne lidar system are in Whiteman et al., (2018). Basically, it consists of the simulation of space-borne multiwavelength High Spectral Resolution Lidar (HSRL) measurements assuming a 1.5 m telescope with field of view of 130 microradians, a Nd:YAG laser operating at 100 Hz with power outputs of 10W at 1064 and 532 nm and 5W at 355 nm. The simulation approach used is described in Whiteman et al., (2001, 2010) and implements the lidar equations and carries all physical units through the entire simulation chain including for background skylight (Measures, 1984). The random uncertainties that are output by the lidar simulator are a direct result of the lidar equation and the assumption of Poisson statistics in the measurement process. The molecular and particle profiles on which the simulations are based come from. Here we work with four different ranges of random uncertainty: from 0-15 %, 15-20 %, 20-30% and 30 - 50%. The performance of the inversions as a function of random uncertainty has a large impact on the yield of a space-borne lidar system (Whiteman et al., 2018) which we will comment on later, but here we will focus on their impact on the retrievals of aerosol microphysical properties.

Table 9 shows the main results of the retrieval of aerosol microphysical properties from simulated space-borne lidar measurements. CDOC were computed and consequently applied to the stand-alone $3\beta+2\alpha$ lidar inversion. The same color-code scheme as for Table 7 has been applied, and also the same ranges of absorption. The results are presented for the four different ranges of random errors.

[Insert Table 9 here]

Table 9 reveals The ability to obtain reliable aerosol microphysical parameters for different ranges of m_i is the largest improvement resulting from the use of CDOC in the space-borne simulations compared with the results discussed in Whiteman et al., (2018) where by default all retrievals operated with $m_{i,max} = 0.01$ and with no limitations in m_r. Moreover, the use of CDOC has particularly allowed the retrievals of aerosol refractive index and SSA, while also improving the general quality of the retrieval of bulk parameters (yellows becoming greens and reds becoming yellows).

For random errors between 0-15% most retrieved parameters are within the uncertainties allowed as most of them fall within the 'green' area. The only exception is SSA at 1064 nm which clearly fails. SSA retrievals at 355 and at 532 nm have significant uncertainties for medium absorption but still fall within the desired range of uncertainty. This increase in uncertainty may be due to the difficulty of associating GEOS data with fine mode predominance or mixture of modes. For uncertainties in the input optical data between 15-20 % the deviation of the retrieved parameters from the reference increase but still remain within the desired range of uncertainty except for SSA(355) for low absorbing case and SSA1064 in general. For uncertainties greater than 20%, the failure rate of the retrievals generally increases considerably with the appearance of many red-coded cells and a larger fraction of yellow-coded cells. The most sensitive retrieved parameters are r_{eff}, m_r and SSA. Degradation of retrievals is more evident as uncertainties in the optical data increase. Such degradations are associated with incorrect selection of constraints that yields to unrealistic retrievals as illustrated in Section 3.1.

Therefore, we conclude that retrievals of space-borne simulations are not feasible for cases when random uncertainties in the input optical data are above 20%.

4.-Discussions, Summary and Conclusions

In this work we have focused on the use of case-dependent optimized-constraints (CDOC) in the stand-alone $3\beta+2\alpha$ lidar inversion. The determination of these constraints from $3\beta+2\alpha$ is possible through the analysis of the spectral dependencies of extinction-to-backscatter ratios (LR) and of the extinction Angstrom exponents. Such computations have been discussed in detail in previous publications and are critical for the retrieval of aerosol refractive index and single scattering albedo (Perez-Ramirez et al., 2019).

Different aerosol and molecular fields generated by the GEOS model have been used here to evaluate the use of CDOC. Our analyses reveal that for cases highly affected by hygroscopic growth the estimation of CDOC cannot be done accurately. We can argue that the GOCART size distributions for hygroscopic growth are not fully realistic considering that AERONET retrievals indicate that the size distributions affected by hygroscopic growth usually possess a larger width and show a change in radius when compared with dry cases (e.g. Schafer et al., 2008). Also, the cut-off established in GOCART where, for fine mode case s(sulphate and carbonaceous species), there are no particles larger than 0.5 μm is not fully consistent with the long-term AERONET database which shows the frequent occurrence of a remnant coarse mode even for fine mode dominated cases (e.g. Dubovik et al., 2002). Actually, the estimation of different aerosol species from remote sensing measurements using the Generalized Retrieval of Atmospheric and Surface Properties (GRASP – Dubovik et al., 2014) always assumes a bimodal size distribution even for cases of fine mode predominance (Chen et al., 2018; Li et al., 2019). Furthermore, the estimation of CDOC fails for cases when pure black carbon is observed (percentage to total mass larger than 7%). Pure black carbon is observed in nature only from measurements in extremely polluted areas. Black carbon quickly interacts with gases through chemical reactions and with other particles through internal mixtures. Because these processes are not included in GOCART, we believe that the refractive index and size distributions for black carbon assumed in GOCART could be unrealistic. We propose further investigations that incorporate typical size distributions and refractive indices observed by AERONET into GOGART in an attempt to reconcile $3\beta+2\alpha$ lidar retrievals from space-borne simulations and modelling.

There are other aerosol size distributions observed in nature that are different from those assumed in the computation of CDOC. Among the most important of these are the tri-modal size distributions typical of fog and cloud-induced aerosol observed from AERONET inversions (Eck et al., 2012). Such size distributions are bimodal in the fine mode (accumulation mode), with one mode in the range 0.4 - 0.5 μm and the other in the range 0.12 - 0.25 μm. A relevant coarse mode centred at ~1.5 μm is also observed. We computed $3\beta+2\alpha$ optical data for this tri-modal size distribution with refractive index m = 1.40 - 0.001i because these cases represent highly hygroscopic aerosols. Such optical data were used as input to the algorithm of Section 2.2 and the data were classified as mixture with low absorption. Therefore, if such tri-modal cases are present, the stand-alone $3\beta+2\alpha$ lidar inversion would retrieve two modes instead. Furthermore, the retrieval of refractive index and SSA are still feasible because the typical tri-modal size distribution corresponds to very low absorption.

We have studied the sensitivity of the estimation of CDOC to uncertainties in the input optical data. A set of unimodal and bimodal size distributions was used to generate the $3\beta+2\alpha$ measurements to which we added both systematic and random components. For random uncertainties we used a Monte Carlo technique and our results indicate that the estimation of CDOC is feasible for random uncertainties below ~ 20%, while for larger errors an incorrect assessment of the aerosol type occurs. On the other hand, we studied the effects of systematic errors by adding systematic biases to the input optical data. To isolate this effect, we fixed the CDOC so they did not vary with changing bias in the optical data. We found generally linear relationships between systematic biases and deviations in the retrieved parameters. For real (m_r) and imaginary (m_i) refractive indices such linear deviations are within the desired limits (± 0.05 for m_r and ±50% for m_i) for biases up to ±30%. Nevertheless, differences can be above the desired limits for biases above ±15% if standard deviations are added to the retrievals. However, we found that retrievals of SSA are particularly sensitive to biases in $\beta(355)$ for biases above ±15%. For size distributions with fine and coarse mode predominance we also observed that biases in $\alpha(355)$ affect the retrievals of SSA, although this sensitivity is lower than that for $\beta(355)$. Therefore, from all these sensitivity tests we can conclude that accurate retrievals by

CDOC are only feasible for random uncertainties in the input optical data below 20%, with the most sensitive optical input being β(355). This result complements the results of Perez-Ramirez et al., (2013) where it was determined that the most sensitive channels for the retrieval of bulk parameters were α(355) and α(532).

We have also analyzed the ability of a simulated space-borne multiwavelength lidar system to retrieve aerosol microphysical properties from the stand-alone 3β+2α lidar inversion when using CDOC. This study is a continuation of the work by Whiteman et al., (2018), who used the stand-alone 3β+2α lidar inversion but limited the maximum m_i to 0.01. Our analyses have allowed the study of the capability of such simulated lidar system to retrieve refractive index and SSA in addition to the parameters studied in Whiteman et al, (2018). Different aerosol and molecular fields were generated by the GEOS model to obtain 3β+2α optical data, and these 3β+2α measurements were then used as inputs to determine CDOC. Those constraints were then used in the regularization retrieval using the GEOS data to represent noise-free lidar simulations. Outputs from the retrievals were then compared with the original GEOS data and the differences analyzed. Our results revealed that such a lidar system is capable of retrieving all bulk parameters (r_{eff}, V, S and N), refractive index (both real and imaginary parts) and SSA at 355 and 532 nm with differences within the desired limits independently of the range of absorption assumed (low absorption with $m_i < 0.01$; medium absorption with $0.01 < m_i < 0.03$; high absorption with $m_i > 0.03$). Further analyses consisted of using the GEOS aerosol and molecular profiles as input to a lidar simulator (Whiteman et al., 2001, 2010) so that realistic uncertainties (up to 50 % in the optical data) could be assigned to the various measurements. These studies revealed that retrieval results using CDOC are still generally within desired limits for random uncertainties up to 20%. For larger errors we observed a degradation of the retrievals mainly in r_{eff} and m_r and SSA, particularly for non-absorbing aerosols.

Our results from space-borne simulations are optimistic about the capabilities of such a system to retrieve aerosol microphysical properties, particularly absorption, using CDOC. But we must be cautious because CDOC are only feasible when uncertainties in the optical data are below 20%. That threshold in the uncertainty limits the yield of the satellite as stated by Whiteman et al., (2018), which claimed for the simulated space-borne lidar system used such uncertainties in optical data of 15% imply a yield of 15% for a 24-hour track satellite (assuming no clouds). Nevertheless, one-to-one comparisons for bulk parameters between the previous study of Whiteman et al., (2018) and the results presented here imply reduced uncertainties in retrieved parameters from 35% to 25% for r_{eff} and from 30 to 25% in surface concentration. Volume concentration uncertainties are very similar between both studies. For m_r, our study represents an advance by allowing retrievals within ±0.03 uncertainty, while the previous work only permitted such retrievals for fine mode predominance and low absorbing aerosol. But the largest achievement presented here is the possibility of retrieving m_i and SSA from spaceborne simulations with reasonable uncertainties (±50% in m_i and ±0.02, ±0.04 and ±0.05 in SSA for low, medium and high absorption, respectively), which has not been demonstrated in previous studies.

In spite of the promising results presented here using CDOC we want to highlight the limitations of such a technique because it is not able to retrieve accurately aerosol microphysical properties in the presence either of highly hygroscopic aerosol or for the case of large differences in the refractive index between fine and coarse modes. Constraining the stand-alone $3\beta+2\alpha$ lidar inversion for these specific cases cannot be done from $3\beta+2\alpha$ measurements alone. The use of additional aerosol depolarization measurements could help for aerosol typing (e.g. Burton et al., 2012, 2013, 2014, 2015) and establishing CDOC for these specific cases. Another current limitation in the use of CDOC is that it is not applicable to dust particles, whose scattering patterns demand the use of more advanced theories such as T-Matrix (e.g. Mischenko and Travis, 1994) and therefore the implementation in the retrievals of non-spherical kernel functions (e.g. Dubovik et al., 2006). Nevertheless, the use of non-spherical kernel functions alone in the stand-alone lidar inversion has been demonstrated as not sufficient for cases when dust particles are in a mixture with other aerosol types (e.g. Veselovskii et al., 2016, 2018), and additional aerosol depolarization measurements are also required. The use of aerosol depolarization measurements will be the focus of future work in lidar inversions and particularly in space-borne systems.

Acknowledgments

This work was supported by the Marie Skłodowska-Curie Research Innovation and Staff Exchange (RISE) GRASP-ACE (grant agreement No 778349), and by the NASA Atmospheric

Composition Program managed by Ken Jucks and by the NASA Aerosols, Clouds, Ecosystems pre-formulation study managed by David Starr and Arlindo Da Silva (ACCP, Scott Braun).

References

Bohren, C.F., and Huffman, D.R. (1998) Absorption and Scattering of light by small particles. Published by WILEY / VCH Verlag GmbH & Co. KGaA, Weinheim.

Burton, S.P., Ferrare, R.A., Hostetler, C.A., Hair, J.W., Rogeres, R.R., Obland, M.D., Obland, M.D., Butler, C.F., Cook, A.L., Harper, D.B., and Froyd., K.D. (2012) Aerosol classification using airborne High Spectral Resolution Lidar measurements - methodology and examples. *Atmospheric Measurement Techniques,* 5, 73-98.

Burton, S.P., Ferrare, R.A., Vaughan, M.A., Omar, A.H., Rogers, R.R., Hostetler, C., and Hair, J.W. (2013) Aerosol classification from airborne HSRL and comparisons with the CALIPSO vertical feature mask. *Atmospheric Measurement Techniques*, 6, 1397-1412.

Burton, S.P., Vaughan, M.A., Ferrare, R.A., Hostetler, C.A. (2014) Separating mixtures of aerosol types in airborne High Spectral Resolution Lidar data. *Atmospheric Measurement Techniques*, 7, 419-436.

Burton, S.P., Hair, J.W., Kahnert, M., Ferrare, R.A., Hostetler, C.A., Cook, A.L., Harper, D.B., Berkoff, T.A., Seaman, S.T., Collins, J.E., Fenn, M.A., and Rogers, R.R. (2015) Observations of the spectral dependence of linear particle depolarization ratio of aerosols using NASA Langley airborne High Spectral Resolution Lidar. *Atmospheric Chemistry and Physics*, 15, 13453-13473.

Burton, S.P., Chemyakin, E., Liu, X., Knobelspiesse, K., Stamnes, S., Sawamura, P., Moore, R.H., Hostetler, C.A., Ferrare, R.A. (2016) Information content and sensitivity of the $3\beta+2\alpha$lidar measurement system for aerosol microphysical retrievals. *Atmospheric Measurement Techniques*, 9, 5555-5574.

Burton, S. P., Hostetler, C. A., Cook, A. L., Hair, J. W., Seaman, S. T., Scola, S., Harper, D. B., Smith, J. A., Fenn, M. A., Ferrare, R. A., Saide, P. E., Chemyakin, E. V., and Müller, D.:

Calibration of a high spectral resolution lidar using a Michelson interferometer, with data examples from ORACLES, *Applied Optics,* 57, 6061-6075, 2018.

Colarco, P.R., Nowottnick, E., Randles, C.A., Yi, B., Yang, P., Kim, K-M., Smith, J.A., and Bardeen, C. (2014) Impact of radiatively interactive dust aerosols in the NASA GEOS-5 climate model: Sensitivity to dust particle shape and refractive index, *Journal of Geophysical Research: Atmospheres*, 119, 753-786.

Chin, M., Ginoux, P., Kinne, S., Torres, O., Holben, B.N., Duncan, B.N., Martin, R.V., Logan, J.A., Higurashi, A., Nakajima, T. (2002) Tropospheric aerosol optical thickness from the GOCART model and comparisons with satellite and sun photometer measurements. *Journal of the Atmospheric Sciences*, 59, 461-483.

Chen, C. Dubovik, O., Henze, D.K., Lapyonak, T., Chin, M., Ducos, F., Litvinov, P., Huang, X., and Li, L. (2018) Retrieval of desert dust and carbonaceous aerosol emission over Africa from POLDER/PARASOL products generated by the GRASP algorithm, *Atmos. Chem. Phys.,* 18, 12551-12580.

Chemyakin, E., Müller, D., Burton, S., Kolgotin, A., Hostetler, R., and Ferrare, R. (2014) Arrange and average algorithm for the retrieval of aerosol parameters from multiwavelength high-spectral-resolution lidar/Raman lidar data. Applied Optics, 53, 7252-7266.

Chemyakin, E., Burton, S., Kolgotin, A., Müller, D., Hostetler, C., and Ferrare, R. (2016) Retrieval of aerosol parameters frommultiwavelengthlidar: investigation of the underlying inverse mathematical problem. Applied Optics, 55, 2188-2202.

Dubovik, O., King, M.D. (2000) A flexible inversion algorithm for retrieval of aerosol optical properties from Sun and sky radiance measurements.*Journal of Geophysical Research*, 105, 20673-20696.

Dubovik, O., Smirnov, A., Holben, B.N., King, M.D., Kaufman, Y., Eck, T.F., and Slutsker, I. (2000) Accuracy assesments of aerosol optical properties retrieved from Aerosol Robotic Network (AERONET) Sun and sky radiance measurements, *Journal of Geophysical Research*, 105, 9791-9806.

Dubovik, O., Holben, B., Eck, T.F., Smirnov, A., Kaufman, Y.J., King, M.D., Tanre, D., Slutsker, I. (2002) Variability of absorption and optical properties of key aerosol types observed in worldwide locations. *Journal of the Atmospheric Sciences,* 59, 590-608.

Dubovik, O., Sinyuk, A., Lapyonok, T., Holben, B.N., Mishchenko, M., Yang, P., Eck, T.F., Volten, H., Muñoz, O., Veihelmann, B., van der Zande, W.J., Leon, J.-F., Sorokin, M., Slutsker, I. (2006) Application of spheroid models to account for aerosol particle nonsphericity in remote sensing of desert dust. *Journal of Geophysical Research*, 111, D11208.

Eck, T.F., Holben, B.N., Reid, J.S., Giles, D.M., Rivas, M.A., Singh, R.P., Tripathi, S.N., Bruegge, C.J., Platnick, S., Arnold, G.T., Krotkov, N.A., Carn, S.A., Sinyuk, A., Dubovik, O., Arola, A., Schafer, J.S., Artaxo, P., Smirnov, A., Chen, H., and Goloub, P. (2012) Fog- and cloud-induced aerosol modification observed by the Aerosol Robotic Network (AERONET), *Journal of Geophysical Research,* 117, D07206

Granados-Munoz, M.J., Bravo-Aranda, J.A., Baumgardner, D., Guerrero-Rascado, J.L., Perez-Ramirez, D., Navas-Guzman, F., Veselovskii, I., Lyamani, H., Valenzuela, A., Olmo, F.J., Titos, G., Andrey, J., Chaikovsky, A., Dubovik, O., Gil-Ojeda, M., and Alados-Arboledas, L. (2016) A comparative study of aerosol microphysical properteis retrieved from ground-based remote sensing and aircraft in situ measurements during a Saharan dust event, *Atmos. Meas. Tech.,* 9, 1113-1133.

Hair, J.W., Hostetler, C.A., Cook, A.L., Harper, D.B., Ferrare, R.A., Mack, T.L., Welch, W., Ramos-Izquierdo, L., Hovis, F., (2008). Airborne High Spectral Resolution Lidar for profiling aerosol optical properties. *Appl. Opt.* 47, 6734–6753.

Li, L., Dubovik, O., Derimian, Y., Schuster, G. L., Lapyonok, T., Litvinov, P., Ducos, F., Fuertes, D., Chen, C., Li, Z., Lopatin, A., Torres, B., and Che, H. (2019) Retrieval of aerosol composition directly from satellite and ground-based measurements, Atmos. Chem. Phys. Discuss., , https://doi.org/10.5194/acp-2019-208

Kolgotin, A., and Müller, D. (2008) Theory of inversion with two-dimensional regularization: profiles of microphysical particle properties derived from multiwavelength lidar measurements. *Applied Optics*, 47, 4472-4490.

Kolgotin, A., Müller, D., Chemyakin, E., and Romanov, A. (2016) Improved identification of the solution space of aerosol microphysical properties derived from the inversion of profiles of lidar optical data, part 1: theory. *Applied Optics*, 55, 9839-9849.

Kovalev, V.A., and Eichinger, W.E. (2004) Elastic Lidar: Theory, practice, and analysis methods. Published by John Wiley & Sons, Inc ., Hoboken, New Jersey.

Loeb, N.G., Su, W. (2010) Direct Aerosol Radiative Forcing Uncertainty Based on a Radiative Perturbation Analysis. *Journal of Climate,* 23, 5288-5293.

Measures RM . Laser remote sensing fundamentals and applications. New York: Wiley; 1984 .

McComiskey, A., Schwartz, S.E., Schmid, B., Guan, H., Lewis, E.R., Ricchiazzi, P., Ogren, J.A. (2008) Direct aerosol forcing: Calculation from observables and sensitivities to inputs. *Journal of Geophysical Research*, 113.

Mishchenko, M.I., Travis, L.D. (1994) Light scattering by polydispersions of randomly oriented spheroids with sizes comparable to wavelengths of observations. *Appl Opt*30, 7206-7225.

Mishchenko, M., I., Travis, L. D., and Lacis, A.A. (2002) Scattering, absorption, and emission of light by small particles. Published by Cambridge University Press, Cambridge.

Mishchenko, M.I., B. Cairns, G. Kopp, C.F. Schueler, B.A. Fafaul, J.E. Hansen, R.J. Hooker, T. Itchkawich, H.B. Maring and L.D. Travis (2007), Accurate monitoring of terrestrial aerosols and total solar irradiance: Introducing the Glory mission, Bull. Amer. Meteorol. Soc., 88, 677-691.

Müller, D., Wandinger, U., and Ansmann, A. (1999a) Microphysical particle parameters from extinction and backscatter lidar data by inversion with regularization: theory, *Applied Optics,* 38, 2346-2368.

Müller, D., Mattis, I., Ansmann, A., Wehner, B., Althausen, D., Wandinger, U., Dubovik, O. (2004) Closure study on optical and microphysical properties of a mixed urban and Arctic haze air mass observed with Raman lidar and Sun photometer. *Journal of Geophysical Research*, 109.

Müller, D., Mattis, I., Wandinger, U., Ansmann, A., Althausen, D. (2005) Raman lidar observations of aged Siberian and Canadian forest fire smoke in the free troposphere over Germany in 2003: Microphysical particle characterization. *Journal of Geophysical Research*, 110.

Müller, D., Kolgotin, A., Mattis, I., Petzold, A., Stohl, A. (2011) Vertical profiles of microphysical particle properties derived from inversion with two-dimensional regularization of multiwavelength Raman lidar data: experiment. *Applied Optics,* 50, 2069-2079.

Noh, Y.M., Müller, D., Shin, D.H., Lee, H., Jung, J.S., Lee, K.H., Cribb, M., Li, Z., Kim, Y.J. (2009) Optical and microphysical properties of severe haze and smoke aerosol measured by integrated remote sensing techniques in Gwangju, Korea. *Atmospheric Environment,* 43, 879-888.

Pérez-Ramírez, D., Whiteman, D.N., Veselovskii, I., Kolgotin, A., Korenskiy, M., Alados-Arboledas, L. (2013) Effects of systematic and random errors on the retrieval of particle microphysical properties from multiwavelengthlidar measurements using inversion with regularization.*Atmospheric Measurement Techniques,* 6, 3039-3054.

Pérez-Ramírez, D., Veselovskii, I., Whiteman, D.N., Suvorina, A., Korenskiy, M., Kolgotin, A., Holben, B., Dubovik, O., Siniuk, A., Alados-Arboledas, L. (2015) High temporal resolution estimates of columnar aerosol microphysical parameters from spectrum of aerosol optical depth by linear estimation: application to long-term AERONET and star-photometry measurements. *Atmospheric Measurement Techniques,* 8, 3117-3133.

Pérez-Ramírez, D., Whiteman, D.N., Veselovskii, I., Colarco, P., Korenskiy, M., and da Silva, A. (2019) Retrievals of aerosol single scattering albedo by multiwavelengthlidar measurements: Evaluations with NASA Langley HSRL-2 during discover-AQ field campaigns, *Remote Sensing of Environment*, 222, 144-164.

Rienecker M , Suarez M , Todling R , Bacmeister J , Takacs L , Liu H-C , et al. The GEOS-5 data assimilation system–documentation of version 5.0.1, 5.1.0, and 5.2.0. In: The GEOS-5 data assimilation system–documentation of version 5.0.1, 5.1.0, and 5.2.0, 27; 2008. p. 1–118. *NASA Technical Report Series on Global Modeling and Data Assimilation* .

Schafer, J.S., Eck, T.F., Holben, B.N., Artaxo, P., and Duarte, F. (2008) Characterization of the optical properties of atmospheric aerosols in Amazonia from long-term AERONET monitoring (1993-1995 and 1999-2006), *Journal of Geophysical Research*, 113, D04204.

Shipley, S.T., Tracy, D.H., Eloranta, E.W., Trauger, J.T., Sroga, J.T., Roesler, F.L., Weinman, J.A. (1983) High spectral resolution lidar to measure optical scattering properties of atmospheric aerosols. 1: Theory and instrumentation. *Applied Optics,* 22, 3716-3724.

Stier, P., Schutgens, N.A.J., Bellouin, N., Bian, H., Boucher, O., Chin, M., Ghan, S., Huneeus, N., Kinne, S., Lin, G., Ma, X., Myhre, G., Penner, J.E., Randles, C.A., Samset, B., Schulz, M., Takemura, T., Yu, F., Yu, H., Zhou, C. (2013) Host model uncertainties in aerosol radiative forcing estimates: results from the AeroCom Prescribed intercomparison study. *Atmospheric Chemistry and Physics*, 13, 3245-3270.

Veselovskii, I., Kolgotin, A., Griaznov, V., Muller, D., Wandinger, U., Whiteman, D. (2002) Inversion with regularization for the retrieval of tropospheric aerosol parameters from multiwavelengthlidar sounding. *Applied Optics*, 41, 3685-3699.

Veselovskii, I., Kolgotin, A., Griaznov, V., Müller, D., Franke, K., and Whiteman, D. (2004) Inversion of multiwavelength Raman lidar data for retrieval of bimodal aerosol size distribution*. Applied Optics*, 43, 1180-1195.

Veselovskii, I., Kolgotin, A., Muller, D., Whiteman, D. (2005) Information content of multiwavelengthlidar data with respect to microphysical particle properties derived from eigenvalue analysis. *Applied Optics*, 44, 5292-5303.

Veselovskii, I., Dubovik, O., Kolgotin, A., Lapyonok, T., Di Girolamo, P., Summa, D., Whiteman, D.N., Mishchenko, M., Tanré, D. (2010) Application of randomly oriented spheroids for retrieval of dust particle parameters from multiwavelengthlidarmeasurements.*Journal of Geophysical Research,* 115, D2103

Veselovskii, I., Dubovik, O., Kolgotin, A., Korenskiy, M., Whiteman, D.N., Allakhverdiev, K., and Huseyinoglu, F. (2012) Linear estimation of particle bulk parameters from multi-wavelength lidar measurements. Atmospheric Measurement Techniques, 5, 1135-1145.

Veselovskii, I., Whiteman, D.N., Korenskiy, M., Kolgotin, A., Dubovik, O., Perez-Ramirez, D., Suvorina, A. (2013) Retrieval of spatio-temporal distributions of particle parameters from multiwavelengthlidar measurements using the linear estimation technique and comparison with AERONET. *Atmospheric Measurement Techniques,* 6, 2671-2682.

Veselovskii, I., Whiteman, D.N., Korenskiy, M., Suvorina, A., Kolgotin, A., Lyapustin, A., Wang, Y., Chin, M., Bian, H., Kucsera, T.L., Pérez-Ramírez, D., Holben, B. (2015) Characterization of forest fire smoke event near Washington, DC in summer 2013 with multi-wavelength lidar. *Atmospheric Chemistry and Physics*, 15, 1647-1660.

Veselovskii, I., Goloub, P., Podvin, T., Bovchaliuk, V., Derimian, Y., Augustin, P., Fourmentin, M., Tanre, D., Korenskiy, M., Whiteman, D.N., Diallo, A., Ndiaye, T., Kolgotin, A., and Dubovik, O. (2016) Retrieval of optical and physical properties of African dust from multiwavelength Raman lidar measurements during the SHADOW campaign in Senegal, *Atmos. Chem. Phys.,* 16, 7013-7028.

Veselovskii, I., Goloub, P., Podvin, T., Tanré, D., da Silva, A., Colarco, P., Castellanos, P., Korenskiy, M., Hu, Q., Whiteman, D.N., Pérez-Ramírez, D., Augustin, P., Fourmentin, M. (2018) Characterization of smoke and dust episode over West Africa: comparison of MERRA-2 modeling with multiwavelength Mie-Raman lidar observations. *Atmospheric Measurement Techniques*, 11, 949-969.

Whiteman, D.N., Pérez-Ramírez, D., Veselovskii, I., Colarco, P., Buchard, V. (2018) Retrievals of aerosol microphysics from simulations of spaceborne multiwavelength lidar measurements*. Journal of Quantitative Spectroscopy &Radiative Transfer,* 205, 27–39 .

Whiteman, D.N., Rush, K.R., Rabenhorst, S., Welch, W., Cadirola, M., McIntire, G., Russo, f., Adam, M., Venable, D., Connell, R., Veselovskii, I., Forno, R., Mielke, B., Stein, B., Leblanc, T., McDermid, S., and Vömel, H. (2010). Airborne and Ground-based measurements using a High-Performance Raman Lidar, Journal of Atmospheric and Oceanic Technoloy, 27, 1781-1801

Whiteman D.N. ,Schwemmer, G., Berkoff, T., Plotkin, H., Ramos-Izquierdo L., Pap-palardo, G. (2001). Performance modeling of an airborne Raman water vapor lidar. *Applied Optics,* 40(3), 375–390 .

Winker, D.M., Pelon, J., Coakley, J.A., Ackerman, S.A., Charlson, R.J., Colarco, P.R., Flamant, P., Fu, Q., Hoff, R.M., Kittaka, C., Kubar, T.L., Le Treut, H., McCormick, M.P., Mégie, G., Poole, L., Powell, K., Trepte, C., Vaughan, M.A., Wielicki, B.A. (2010) The CALIPSO Mission: A Global 3D View of Aerosols and Clouds. *Bulletin of the American Meteorological Society*, 91, 1211-1229.

Yorks, J.E., McGill, M.J., Palm, S.P., Hlavka, D.L., Selmer, P.A., Nowottnick, E.P., Vaughan, M.A., Rodier, S.D., Hart, W.D. (2016) An overview of the CATS level 1 processing algorithms and data products. *Geophysical Research Letters*, 43, 4632-4639.

Zarzycki, C.M., and Bond, T.C. (2010) How much can the vertical distribution of black carbon affect its global direct radiative forcing?,*Geophysical Research Letters,* 37, L20807.

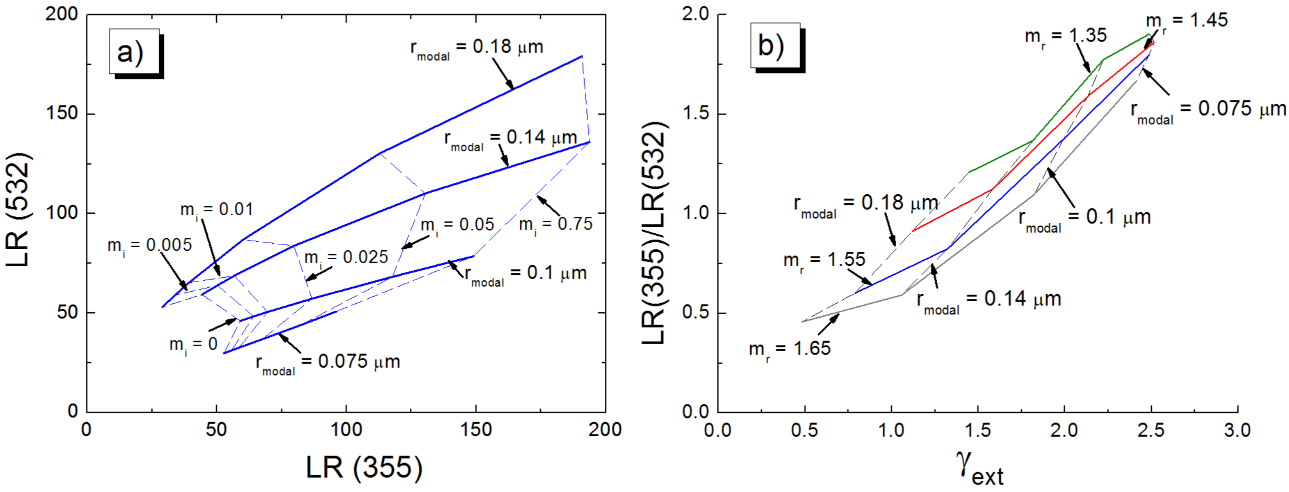

Figure 1: (a) Spectral dependence of extinction-to-backscattering ratio (LR) for fixed unimodal size distributions of r_{modal} = 0.075, 0.10, 0.14, and 0.18 μm, m_i= 0, 0.005, 0.01, 0.025, 0.05 and 0.075 and fixed m_r = 1.55. (b) Ratio of the extinction-to-backscattering ratios versus the Angström exponent of extinction (γ_α) or r_{modal} = 0.075, 0.10, 0.14, and 0.18 μm and m_r = 1.35, 1.45, 1.55 and 1.65 and fixed m_i = 0.01.

Figure 2: Deviations of the single scattering albedo (ΔSSA) at 355 nm as function of systematic bias in the optical data (Δε) for (a) low (b) medium and (c) high absorbing aerosol. ACE error limits for SSA are approximately of ±0.02, ±0.04 and ±0.05 for low, medium and high absorption, respectively.

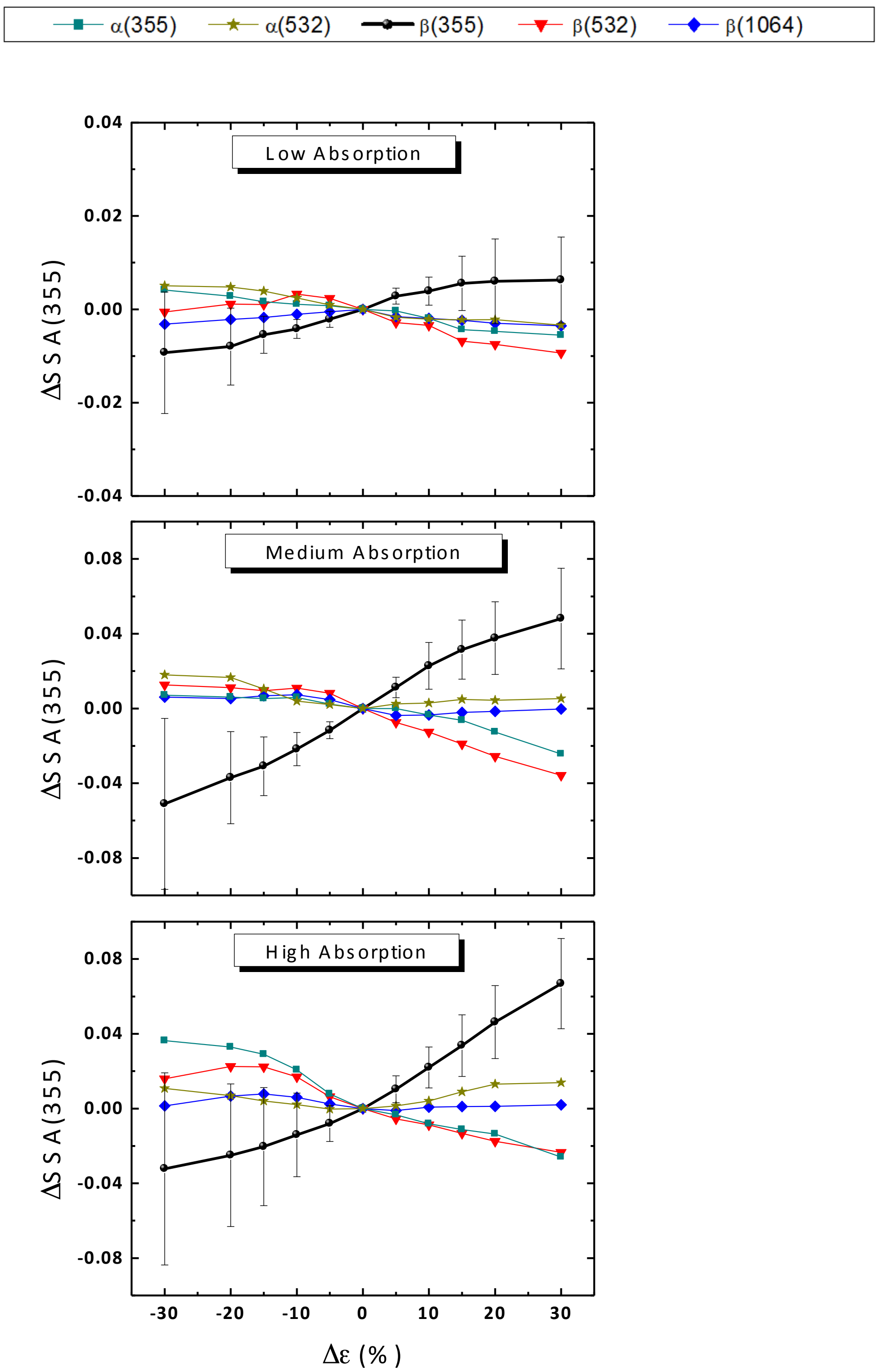

Figure 2: Deviations of the single scattering albedo (ΔSSA) at 355 nm as function of systematic bias in the optical data (Δε) for (a) low (b) medium and (c) high absorbing aerosol. ACE error limits for SSA are approximately of ±0.02, ±0.04 and ±0.05 for low, medium and high absorption, respectively.

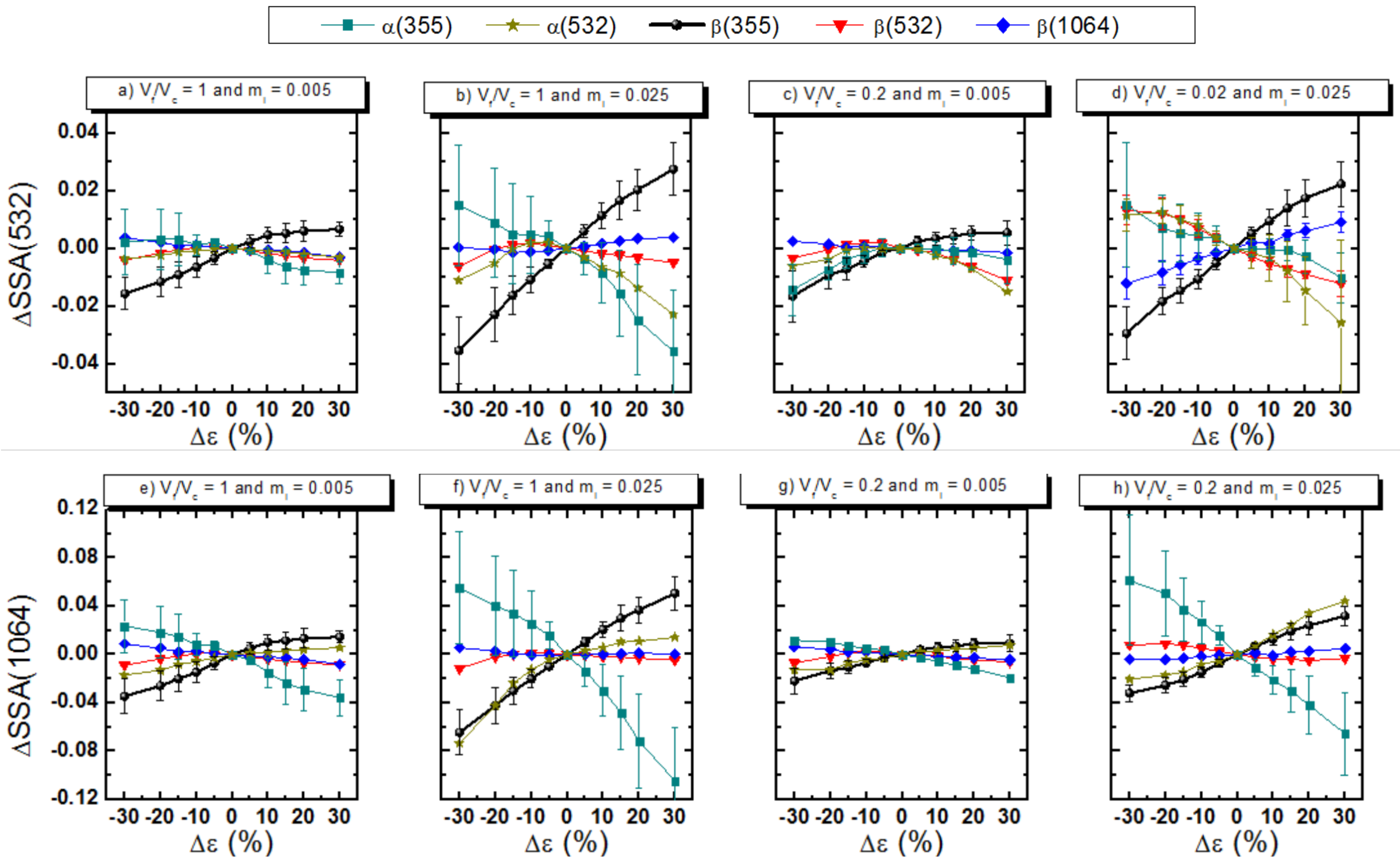

Figure 3: Deviations of the single scattering albedo (ΔSSA) as function of systematic bias in the optical data (Δε) for bimodal size distributions with different fine-to-coarse volume ratios (V_f/V_c) and imaginary refractive index m_i(a)-(d) at 532 nm, (e)-(f)at 1064 nm. ACE error limits for SSA are approximately of ±0.02, ±0.04 and ±0.05 for low, medium and high absorption, respectively.

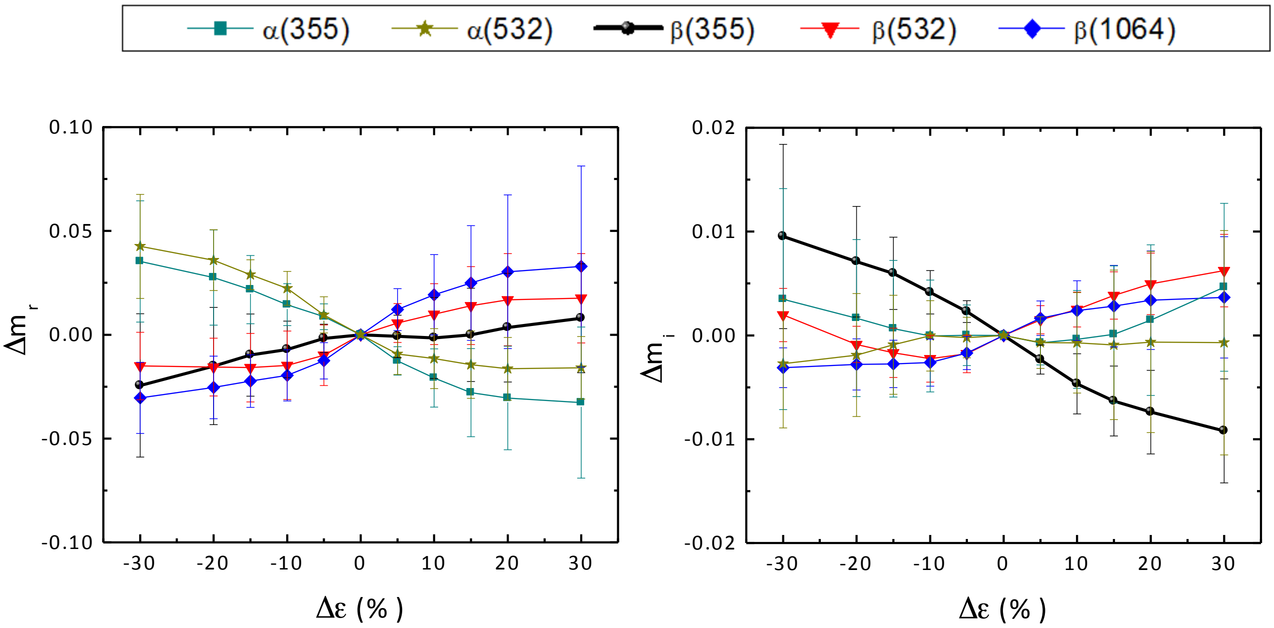

Figure 4: Deviations of the real and imaginary (Δm_i) part of refractive indexas function of systematic bias in the optical data ($\Delta\varepsilon$) for the case of fine mode predominance and medium absorption. Results represented are for medium absorption with m_i = 0.025 for generating optical data. ACE error limits for m_r are of and for m_i ±0.01 for absorption.

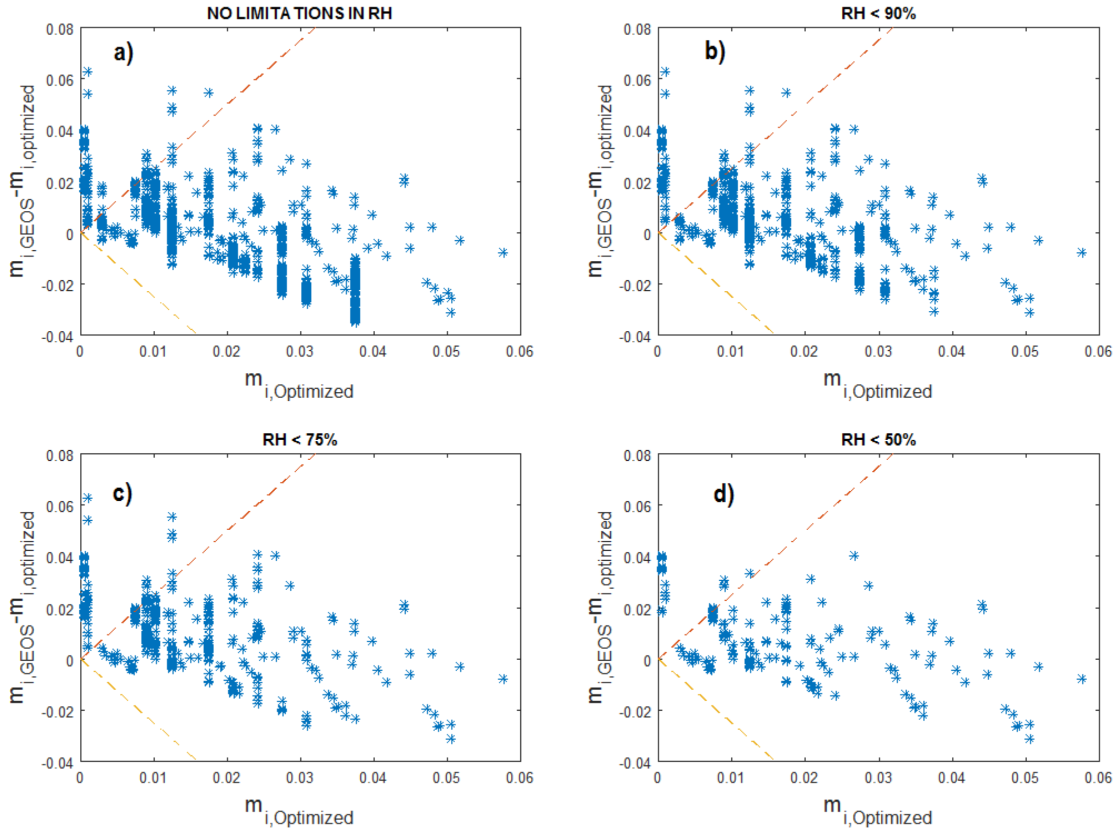

Figure 4: Differences between GEOS imaginary refractive index ($m_{i,GEOS}$) and optimized refractive index ($m_{i,optimized}$) as function of $m_{i,optimized}$. Dashed lines represent $\pm 2.5 m_{i,optimized}$ which is the optimal range for the stand-alone lidar inversion. Different ranges of relative humidity (RH) in GEOS are considered (a) no limitation in RH, (b) RH < 90%, (c) RH < 75% and (d) RH < 50%.

	CASE OF FINE MODE PREDOMINANCE AND LOW ABSORPTION AS INPUT				
Uncertainties in the optical data	Classified as Fine Mode Predominance			Classified as Mixture of Modes	
	Low Absorption	Medium Absorption	High Absorption	Low Absorption	Medium Absorption
5 %	95.6 %	3.6 %	0 %	0.8 %	0 %
10 %	78.9 %	17.1 %	0 %	4.1 %	0 %
20 %	65.5 %	18.8 %	0.8 %	13.5 %	0.2 %
30 %	58.7 %	12.8 %	1.3 %	25.1 %	2.2 %
50 %	54.5 %	6.6 %	1.6 %	32.9 %	4.5 %

	CASE OF FINE MODE PREDOMINANCE AND MEDIUM ABSORPTION AS INPUT				
Uncertainties in the optical data	Classified as Fine Mode Predominance			Classified as Mixture of Modes	
	Low Absorption	Medium Absorption	High Absorption	Low Absorption	Medium Absorption
5 %	7.1 %	91.4 %	0 %	1.4 %	0.2 %
10 %	10.8 %	73.5 %	1.2 %	11.8 %	2.8 %
20 %	5.3 %	43.8 %	12.5 %	29.7 %	8.8 %
30 %	2.2 %	25.9 %	17.3 %	39.0 %	15.7 %
50 %	0.9 %	12.0 %	17.3 %	46.7 %	23.3 %

	CASE OF FINE MODE PREDOMINANCE AND HIGH ABSORPTION AS INPUT				
Uncertainties in the optical data	Classified as Fine Mode Predominance			Classified as Mixture of Modes	
	Low Absorption	Medium Absorption	High Absorption	Low Absorption	Medium Absorption
5 %	0 %	1.2 %	97.8 %	0 %	0 %
10 %	0 %	3.3 %	95.5 %	0.5 %	0.7 %
20 %	0.2 %	7.8 %	78.8 %	6.2 %	6.9 %
30 %	0.4 %	7.9 %	61.4 %	14.7 %	15.7 %
50 %	0.5 %	5.7 %	41.4 %	30.0 %	22.8 %

	CASE OF MIXTURE OF MODES AND LOW ABSORPTION AS INPUT				
Uncertainties in the optical data	Classified as Fine Mode Predominance			Classified as Mixture of Modes	
	Low Absorption	Medium Absorption	High Absorption	Low Absorption	Medium Absorption
5 %	0.4 %	0.0 %	0.0 %	80.3 %	19.4 %
10 %	8.7 %	0.2 %	0.0 %	70.8 %	20.4 %
20 %	24.6 %	0.5 %	0.0 %	55.4 %	15.1 %
30 %	32.4 %	5.5 %	0.1 %	48.1 %	14.0 %
50 %	38.6 %	4.8 %	0.5 %	44.0 %	12.0 %

	CASE OF MIXTURE OF MODES AND MEDIUM ABSORPTION AS INPUT				
Uncertainties in the optical data	Classified as Fine Mode Predominance			Classified as Mixture of Modes	
	Low Absorption	Medium Absorption	High Absorption	Low Absorption	Medium Absorption
5 %	0.2 %	0.0 %	0.0 %	8.9 %	90.9 %
10 %	10.7 %	0.1 %	0.0 %	24.7 %	64.6 %
20 %	24.3 %	4.3 %	0.0 %	32.4 %	39.1 %
30 %	32.8 %	5.5 %	0.0 %	34.9 %	26.7 %
50 %	40.0 %	3.8 %	0.0 %	35.4 %	20.9 %

Table 1: Sensitivity of the computation of $m_{i,optimized}$ and the range of inversion for the computation of case-dependent optimized-constraints to random uncertainties in the input optical data.

	Aerosol Type	SSA_{355}	SSA_{532}	SSA_{1064}	m_r	m_i
5 % Random Uncertainties	**Fine - Low Abs.**	0.01	0.02	0.04	0.03	0.001
	Fine - Medium Abs.	0.03	0.03	0.05	0.04	0.005
	Fine -High Abs	0.03	0.03	0.04	0.01	0.011
	Mixture - Low Abs.	0.06	0.03	0.02	0.05	0.007
	Mixture - Medium Abs	0.07	0.04	0.03	0.04	0.006
10 % Random Uncertainties	**Fine - Low Abs.**	0.02	0.02	0.06	0.05	0.005
	Fine - Medium Abs.	0.04	0.04	0.08	0.05	0.009
	Fine -High Abs	0.04	0.05	0.07	0.03	0.011
	Mixture - Low Abs.	0.07	0.03	0.02	0.06	0.007
	Mixture - Medium Abs	0.08	0.04	0.04	0.06	0.010
15 % Random Uncertainties	**Fine - Low Abs.**	0.02	0.03	0.08	0.03	0.005
	Fine - Medium Abs.	0.03	0.04	0.10	0.04	0.010
	Fine -High Abs	0.04	0.05	0.12	0.05	0.015
	Mixture - Low Abs.	0.09	0.03	0.03	0.03	0.005
	Mixture - Medium Abs	0.12	0.05	0.04	0.05	0.010
20 % Random Uncertainties	**Fine - Low Abs.**	0.10	0.12	0.21	0.06	0.007
	Fine - Medium Abs.	0.07	0.08	0.16	0.06	0.016
	Fine -High Abs	0.21	0.25	0.49	0.05	0.022
	Mixture - Low Abs.	0.08	0.07	0.05	0.07	0.008
	Mixture - Medium Abs	0.10	0.06	0.06	0.07	0.012
50 % Random Uncertainties	**Fine - Low Abs.**	0.25	0.15	0.44	0.07	0.010
	Fine - Medium Abs.	0.13	0.15	0.45	0.08	0.024
	Fine -High Abs	0.52	0.45	0.12	0.07	0.029
	Mixture - Low Abs.	0.46	0.24	0.12	0.08	0.009
	Mixture - Medium Abs	0.40	0.12	0.10	0.07	0.011

Table 2: Standard deviations in spectral single scattering albedo (SSA) and in complex refractive index ($m = m_r - im_i$) for different aeroso types after running the $3\beta+2\alpha$ lidar inversion with case-dependent optimized-constraints computed with random uncertainties in the optical data.

		Standard Deviations of ΔSSA with different systematic uncertainties in the input optical data				
		5 %	**10 %**	**15 %**	**20 %**	**30 %**
SSA(355)	**Low**	0.01-0.02	0.01-0.03	0.01 – 0.04	0.01 – 0.05	0.01 – 0.06
	Medium	0.01-0.02	0.01-0.03	0.01 – 0.04	0.01 – 0.05	0.02 – 0.06
	High	0.01-0.02	0.01 – 0.04	0.01 – 0.04	0.01 – 0.05	0.02 – 0.06
SSA(532)	**Low**	0.01-0.02	0.01-0.03	0.01 –0.05	0.01 – 0.06	0.02 – 0.07
	Medium	0.01 – 0.02	0.01 – 0.04	0.01 -0.05	0.01 – 0.06	0.02 – 0.08
	High	0.01 -0.02	0.01 – 0.05	0.02 – 0.06	0.02 -0.07	0.03 – 0.08
SSA(1064)	**Low**	0.01 - 0.02	0.01 – 0.03	0.01 – 0.03	0.01 - 0.04	0.01 – 0.05
	Medium	0.01 – 0.03	0.02- 0.05	0.02 – 0.08	0.02 – 0.10	0.04 – 0.14
	High	0.01 - 0.03	0.02 – 0.04	0.02 – 0.07	0.03 – 0.08	0.04 – 0.10

Table 3: Standard deviations of the differences in single scattering albedo (SSA) when optical data are affected by systematic uncertainties. Results are for fine mode predominance cases and include different ranges of absorption. Minima are associated with the least sensitive optical data and maxima with the most sensitive optical data.

			Standard Deviations of ΔSSA at different biases in the optical data				
			5 %	**10 %**	**15 %**	**20 %**	**30 %**
$V_f/V_c = 1$	**SSA(355)**	**Low**	0.01	0.01	0.01	0.01	0.01
		Medium	0.01	0.01	0.01	0.01-0.02	0.01-0.04
	SSA(532)	**Low**	0.01	0.01	0.01	0.01	0.01
		Medium	0.01	0.01-0.02	0.01-0.02	0.01-0.02	0.01-0.04
	SSA(1064)	**Low**	0.01	0.01	0.01-0.02	0.01-0.03	0.01-0.04
		Medium	0.01-0.02	0.01-0.02	0.01-0.05	0.01-0.07	0.01-0.10
$V_f/V_c = 0.2$	**SSA(355)**	**Low**	0.01	0.01	0.01	0.01	0.01
		Medium	0.01	0.01	0.01-0.02	0.01-0.06	0.01-0.15
	SSA(532)	**Low**	0.01	0.01	0.01	0.01	0.01-0.2
		Medium	0.01	0.01	0.01	0.01-0.02	0.01 – 0.02
	SSA(1064)	**Low**	0.01	0.01	0.01	0.01-0.02	0.01-0.02
		Medium	0.01	0.01-0.02	0.01-0.03	0.01-0.04	0.01-0.7

Table 4: Standard deviations of the differences in single scattering albedo (SSA) when data are affected by systematic uncertainties in the input optical data. Results are for different fractions between fine and coarse mode volumes (V_f/V_c) and for low ($m_i<0.01$) and medium absorptions ($0.01<m_i<0.03$). Minima are associated with the less sensitive optical data and maximum with the most sensitive optical data.

		Effective Radius	Number	Surface	Volume
α(355)	**Low**	-1.41 ± 0.16	3.39 ± 0.21	1.80 ± 0.05	0.82± 0.06(p) / 0.28 (n) ±0.012
	Medium	-0.85 ± 0.03(p)/ -1.92 ±0.17 (n)	3.17 ± 0.21	1.85 ± 0.07	0.77±0.05(p) / 0.10 (n) ± 0.17
	High	-0.99 ± 0.03 (p)/ -3.3 ± 0.3 (n)	2.74 ± 0.21	1.83 ± 0.07	0.41± 0.10(p) / -0.46 (n) ± 0.17
α(532)	**Low**	1.33 ± 0.09	-2.89 ± 0.26	-0.94 ± 0.08	0.31 ± 0.09
	Medium	1.34 ± 0.06	-2.56 ± 0.28	-0.82 ± 0.08	0.51 ± 0.06
	High	1.54 ± 0.06	-1.66± 0.28	-0.59 ± 0.05	0.98 ± 0.05
β(355)	**Low**	-0.15 ± 0.01	-0.13 ± 0.05 (p)/ -0.97 ±0.09 (n)	-0.47 ± 0.04	-1.39 ± 0.04
	Medium	0.05 0.01	-0.37 ± 0.07 (p)/ -1.28 ±0.04 (n)	-0.40 ± 0.03	-0.36 ± 0.03 (p)/ -0.99 ±0.09 (n)
	High	0.15 ± 0.03	-0.53 ± 0.03 (p)/ -0.11 ±0.02 (n)	0.01 ± 0.02	0.15 ± 0.03
β(532)	**Low**	0.27 ± 0.04	1.88 ±0.16	1.00 ± 0.02 (p)/ 0.34 ±0.04 (n)	0.70 ± 0.02 (p)/ -0.16 ±0.03 (n)
	Medium	-0.24 ± 0.01	1.87 ±0.21	0.79 ± 0.02 (p)/ 0.16 ±0.04 (n)	0.36 ± 0.04 (p)/ -0.04 ±0.01 (n)
	High	-0.12 ± 0.03	1.22 ±0.07	0.25 ± 0.03 (p)/ 0.18 ±0.01 (n)	0.01 ± 0.04
β(1064)	**Low**	0.21 ± 0.02	-0.38 ± 0.06 (p)/ -1.71 ±0.22 (n)	-0.24 ± 0.02	-0.03 ± 0.04
	Medium	0.17 ± 0.02	-0.43 ± 0.04 (p)/ -1.96 ±0.40 (n)	-0.31 ± 0.04	0.58 ± 0.05
	High	0.06 ± 0.03	-0.04 ± 0.08 (p)/ -0.41 ±0.04 (n)	-0.27 ± 0.03	0.28 ± 0.05

Table 5: Percentage deviations in the aerosol bulk parameters as a function of systematic uncertainties in the optical data $\Delta\varepsilon$. Particularly, the slopes 'a' of the linear fits Y = aX are presented, where 'X' is the systematic bias in the optical data and Y is the corresponding deviation in the microphysical properties. All these fits presented linear determination coefficient R^2> 0.95. For the cases when there is a difference in slope between positive and negativethe slopes relating to positive biases are indicated by (p), while those for negative biaseses are indicated by (n).

r_{modal} (µm)	σ (µm)	LR355 (sr)	LR532 (sr)	γα	AEROSOL TYPE
0.12	0.4	77.9	61.0	1.9	Fine and low absortion
0.16	0.4	109.7	89.2	1.7	Fine and low absorption
	0.6	105.8	93.6	1.2	Fine and low absorption
	0.8	92.1	91.9	0.9	Fine and low absorption
0.20	0.4	116.8	102.4	1.3	Fine and low absorption
	0.6	105.2	102.1	1.0	Fine and medium absorption
	0.8	87.8	93.4	0.7	Fine and medium absorption
0.25	0.4	121.1	111.1	0.9	Mixture and medium absorption
	0.6	98.4	106.1	0.7	Mixture and Medium Absorption
	0.8	81.2	91.5	0.5	Mixture and medium absorption
0.30	0.4	117.6	116.9	0.6	Fine and high absorption
	0.6	88.8	105.5	0.5	Mixture and medium absorption
	0.8	74.9	87.8	0.4	Mixture and medium absorption

Table 6: Extinction-to-backscattering ratios (LR) and Angström exponent (γα) of extinction for different monomodal aerosol size distributions varying modal radius (r_{modal}) and width (σ). Also, is shown the aerosol type classification using the algorithm of section 3.1.

	Relative Differences			Absolute Differences				
	r_{eff}	V	S	m_r	m_i	SSA355	SSA532	SSA1064
m_i< 0.01	14.6	16.7	22.2	0.03	0.003	0.02	0.02	0.03
0.01 < m_i< 0.03	11.4	13.8	22.3	0.03	0.007	0.03	0.03	0.08
m_i> 0.03	16.4	8.7	22.8	0.02	0.02	0.04	0.04	0.08

Table 7: Comparison of GEOS-5 aerosol bulk parameters, refractive index and spectral single scattering albedo and the values obtainted from the stand-alone 3β+2α lidar inversion with case-dependent optimized-constraints using GEOS-5 optical data as input. The values shown are root-mean-squares defined in Eqs. (2) and (3). In the column headings the range of absorption is also defined.

		Error allowed per color-code		
		Green	**Yellow**	**Red**
Effective Radius		≤ 25 %	25 – 40%	≥ 40 %
Volume Concentration		≤ 20 %	20 - 35%	≥ 35 %
Surface Concentration		≤ 25 %	25 – 40%	≥ 40 %
Real refractive Index		≤ 0.03	0.03 – 0.05	≥ 0.05
Imaginary refractive index	$\mathbf{m_i < 0.01}$	≤ 0.005	0.005-0.007	≥ 0.007
	$\mathbf{0.01 < m_i < 0.03}$	≤ 0.01	0.01-0.02	≥ 0.02
	$\mathbf{m_i > 0.03}$	≤0.015	0.015-0.03	≥ 0.03
Single Scattering albedo	$\mathbf{m_i < 0.01}$	≤0.02	0.03	≥ 0.04
	$\mathbf{0.01 < m_i < 0.03}$	≤ 0.03	0.04	≥ 0.05
	$\mathbf{m_i > 0.03}$	≤ 0.04	0.05	≥ 0.06

Table 8: Color schme used for Tables 7 and 9. Green indicates values fully consistent with uncertainties expected in retrieved parameters. Yellow indicates uncertainties marginally consistent and red indicates values above the allowed uncertainties.

		Relative Differences			Absolute Differences				
		r_{eff}	V	S	m_r	m_i	SSA355	SSA532	SSA1054
Error 0-15%	$m_i \leq 0.01$	25	15	25	0.03	0.005	0.02	0.03	0.03
	$0.01 < m_i < 0.03$	20	16	23	0.03	0.009	0.04	0.04	0.17
	$m_i \geq 0.03$	30	15	20	0.03	0.012	0.04	0.04	0.11
Error 15-20%	$m_i \leq 0.01$	25	35	27	0.04	0.002	0.04	0.03	0.06
	$0.01 < m_i < 0.03$	30	12	29	0.03	0.012	0.04	0.04	0.05
	$m_i \geq 0.03$	20	19	30	0.04	0.018	0.05	0.05	0.07
Error 20-30%	$m_i \leq 0.01$	56	63	27	0.05	0.002	0.05	0.04	0.04
	$0.01 < m_i < 0.03$	27	19	36	0.05	0.013	0.04	0.04	0.05
	$m_i \geq 0.03$	36	15	30	0.06	0.016	0.05	0.05	0.1
Error 30-50%	$m_i \leq 0.01$	72	74	27	0.09	0.004	0.07	0.06	0.04
	$0.01 < m_i < 0.03$	51	20	40	0.04	0.012	0.04	0.06	0.10
	$m_i \geq 0.03$	60	14	29	0.09	0.025	0.06	0.06	0.18

Table 9: Comparison of GEOS-5 aerosol bulk parameters, refractive index and spectral single scattering albedo and retrieved values from the stand-alone $3\beta+2\alpha$ lidar inversion with case-dependent optimized-constraints using simulated space-borne lidar measurements. Cases are again separated into different ranges of absorption and random uncertainties in the input optical data of the space-borne lidar system.